TENSION-INDUCED TUNABLE CORRUGATION IN TWO-PHASE SOFT COMPOSITES AND ITS PROPERTIES AS A BAND GAP STRUCTURE

BY

QIANLI CHEN

THESIS

Submitted in partial fulfillment of the requirements
for the degree of Master of Science in Civil Engineering
in the Graduate College of the
University of Illinois at Urbana-Champaign, 2015

Urbana, Illinois

Advisor:

Professor Ahmed Elbanna

ABSTRACT

This thesis numerically investigates the elastic deformation response of a two-phase soft composite under externally applied concentric tension and its properties as a band gap structure. By carefully designing the inclusion pattern, it is possible to induce corrugations normal to the direction of stretch. By stacking 1D composite fibers to form 2D membranes, these corrugations collectively lead to the formation of membrane channels with shapes and sizes tunable by the level of stretch and enable the interfaces to progressively soften and evolve into non-planar geometries characterized by the nucleation and stable growth of interfacial channels of irregular shapes. It is also possible to modulate the band gap profile of the composite structure as a result of interfacial deformations and the corresponding microstructural evolution. Furthermore, by using specific inclusion patterns in laminated plates, it is possible to create pop-ups and troughs enabling the development of complex 3D geometries from planar construction. The corrugation amplitude increases with the stiffness of inclusion and its eccentricity from the tension axis. The techniques discussed in this thesis provide greater flexibility and controllability in pattern design and have potential applications in providing a novel framework for harnessing controlled damage in the development of targeted acoustic band gaps and optimizing damping properties of composites.

ACKNOWLEDGEMENTS

Foremost, I would like to express my sincere gratitude to my advisor Prof. Ahmed Elbanna for the continuous support of my M.S. study and research, for his patience, motivation, enthusiasm, and immense knowledge. His guidance helped me in all the time of research and writing of this thesis.

I would like to thank the Department of Civil and Environmental Engineering at University of Illinois at Urbana Champaign for providing the high quality of education courses and academic resources. I am also grateful to all colleagues in our group for offering suggestions and help to my research.

Last but not the least, I would like to thank my family: my parents Haijun Chen and Yunsu Zhang, for giving birth to me at the first place and supporting me spiritually throughout my life.

Table of Contents

CHAPTER 1

INTRODUCTION

Composites are frequently found as building blocks of tough biological structures[1]–[4]. Among those, bone is a typical example exhibiting remarkable combination of stiffness and toughness[5]. The basic block of bone at the micro scale is the mineralized collagen fibril (MCF) in which the soft collagen matrix is reinforced by stiff hydrated calcium phosphates[6]. The MCFs are glued together using interfaces of non-collagenous proteins with sacrificial bonds and hidden length structure[7]–[10]. Another example is seashell nacre which endows dramatic improvement of stiffness and toughness compared to its constituent phases independently[11]. The enhancement of toughness in those biological materials is partially attributed to wavy surfaces and cohesive interaction along the interfaces between bulk materials[12]–[14]. These interfaces are sacrificial in the sense that they represent weak spots where energy gets dissipated by progressive accumulation of damage while the rest of the composite remains intact and elastic. The naturally optimized properties of stiffness, strength, and toughness, suggest that there is a link between geometric patterning, sacrificial interfaces, and improved mechanical performance. More recently, it has also been hypothesized that the origin of these improved properties may be linked to the ability of generating multiple band gaps[15].

Developing complex and 3D controllable geometries, especially at nano and micro scales, is a

topic of immense interests in a variety of fields[16]–[19]. Significant progress has been made in that field in the last 10 years with the advancement of 3D printing techniques[20] as well as the exploitation of certain mechanical effects such as compressive buckling[18]. Here we show, numerically, that the application of a tensile loading to a reinforced elastomeric fiber with designed inclusion patterns induces local bending deformation modes in the form of corrugations normal to the load application directions. By controlling the distribution of the stiff inclusions within the soft matrix, in a way that is inspired by the staggered patterns of elongated mineral particles in MCF, we are able to control the location, amplitude, and wavelength of these corrugations. This opens new opportunities for hierarchical material design in 2D and 3D.

Composite materials with periodic microstructure are capable of generating a band gap structure through which elastic and acoustic wave propagation may be controlled[21]–[25]. Waves with frequencies falling into the band gap are barred by the periodic structure. The band gap phenomenon in composite material is caused by to two mechanisms: Bragg diffraction and local resonance[26], [27]. The Bragg diffraction occurs when the elastic wave length is comparable to the periodicity of the microstructure. The position and the width of the band gap may be controlled by careful design of the microstructure materials[28]–[31]. Moreover, mechanically triggered large deformation[32] and instability-induced interfacial wrinkling[33], [34] are found of capacity to tune the evolution of band gap profile. Local resonance happens when the phases of composite material have strong elastic properties contrast. Banded frequencies caused by local resonance are generally lower than those caused by Bragg

diffraction[35] and may exist even in absence of periodicity and symmetry [26], [36]. Designing such band gap structures enables the application of wave filtering, wave guiding, acoustic mirrors and vibration isolators[37]–[43].

The remainder of this thesis is organized as follows. We describe the material model and the numerical algorithm for modeling both uniaxial stretch and wave propagation in Chapter 2. We summarize our results related to tension-induced corrugations in 1D, 2D, and 3D in Chapter 3. There we examine the different factors affecting the corrugation amplitude such as the elastic moduli ratio of the composite constituents, the aspect ratio of the mineral plates and their location relative to the fibril axis. Then, in Chapter 4, we investigate the changes in the dispersion diagrams as a function of stretch. We consider both the monolithic and layered composites. We also give the evolution of band gap structure as a function of stretch for different composite microstructure and cohesive interfaces properties. In Chapter 5, we conclude by discussing the main findings, and potential applications.

CHAPTER 2

THEORY AND SIMULATION

2.1 Geometry and FEM

Our starting point is a long and slender polymer fibril (Fig.1) of total length L and depth h $(L \gg h)$. The fibril is reinforced with two rows of staggered platelets with length L_i, width t, offset $c + t/2$ from the fibril axis and inter-platelet spacing $L_i + 2s$. If $s < 0$, the platelets in the two rows are overlapping. A typical unit cell representing the fibril composition is shown in Fig. 1. We choose $L = 1000 \ll m$, $h = 30 \ll m$ and $t = 7.5 \ll m$ for manufacturing convenience but specific values are irrelevant since elasticity equations are scale free. We vary the remaining parameters in a controlled way to explore the design space. We choose micrometer ($\ll m$) as a unit of length, and Giga Pascal (GPa) as a unit of stress.

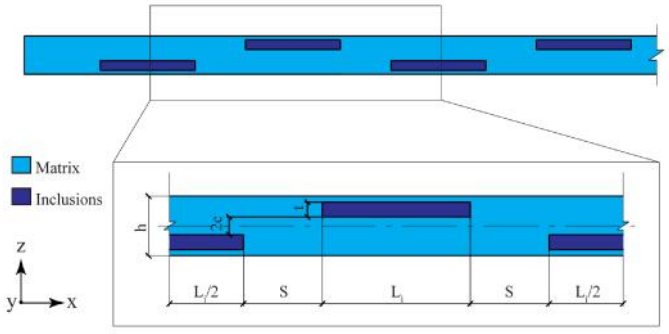

Fig. 1 Geometrical dimensions of unit cell of single composite fibril.

We construct 2D membranes and 3D plates using the composite fibril as a template. Two examples are shown in Fig. 2. The 2D membrane is constructed by gluing the fibrils along their longer edges using a weak polymeric adhesive. The 3D composite plate is constructed by extruding the fibril in the y-direction (normal to the plane of 2D model in Fig.2a). The inclusions are represented by square plates of thickness *t*.

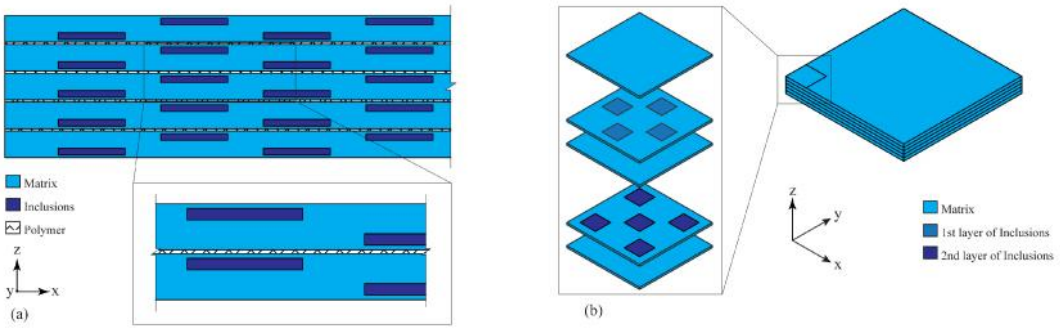

Fig. 2 Geometrical illustration of (a) 2D membranes and (b) 3D plates.

For band gap structure, we consider layered composites made up of stacks of fibrils that are glued along their longer dimension as shown in Fig.3. We choose fibril thickness $h = 30\text{«}m$, length of inclusion $L_i = 75\text{«}m$, inclusion thickness $t = 7.5\text{«}m$, inclusion spacing $S = 40\text{«}m$ and inclusion eccentricity from center line of fibril $c = 4.5\text{«}m$. We consider two types of inclusion pattern: (1) symmetrically aligned inclusions (Fig. 3a), and (2) staggered inclusions (Fig. 3b). An extensive analysis of the effect of geometry and material properties on the response of these composites under longitudinal stretch are reported in a previous paper[44]. The unit cell is discretized using 8-node bi-quadrilateral elements (Q8). Reduced integration is applied for quadrature and the nonlinear problem is solved with full Newton Raphson method.

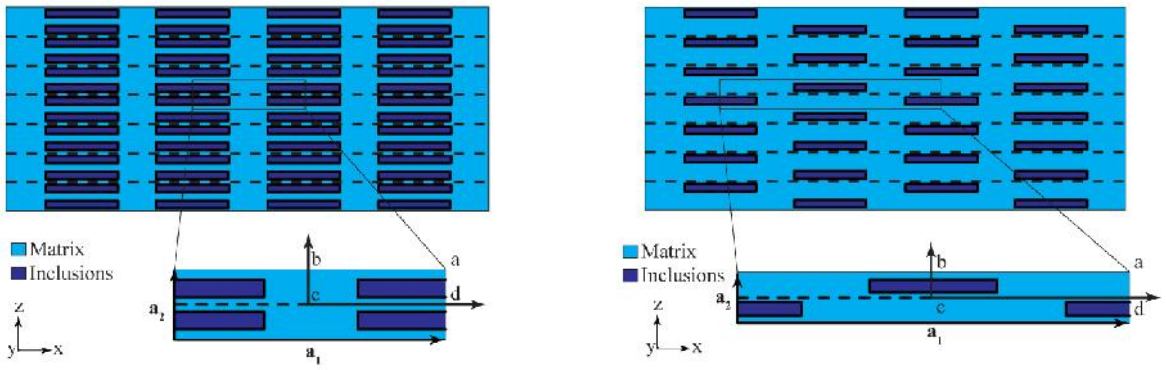

(a) (b)

Fig. 3 Representative unit cell of (a) composite with symmetrically aligned inclusion pattern and (b) composite with staggered inclusion pattern (dashed lines indicate the cohesive interfaces which do not exist in monolithic models).

2.2 Constitutive laws

The material deformation is described as a mapping from reference configuration $\mathbf{X}$ to the deformed configuration $\mathbf{x}$

$$\mathbf{x} = \chi(\mathbf{X}, t), \tag{1}$$

The displacement of a material point form is

$$\mathbf{u} = \mathbf{x} - \mathbf{X} = \chi(\mathbf{X}, t) - \mathbf{X}. \tag{2}$$

The deformation gradient tensor is defined as

$$\mathbf{F} = \frac{\partial \mathbf{x}}{\partial \mathbf{X}} = \mathbf{I} + \frac{\partial \mathbf{u}}{\partial \mathbf{X}}, \tag{3}$$

where $\mathbf{I}$ is the identity matrix and its Jacobian is $J = \det(\mathbf{F})$.

Two different soft materials are building up the composite (Fig. 3). Each material is assumed to be homogeneous and isotropic with hyperelastic response. We use the generalized Neo-Hookean solid[45], [46] model with strain energy density proposed by

$$W = \frac{\alpha}{2}(\bar{I}_1 - 3) + \frac{K}{2}(J-1), \tag{4}$$

where $\bar{I}_1 = I_1 / J^{2/3}$ making it more convenient for nearly incompressible materials, α and K are the shear modulus and bulk modulus of the material respectively.

The stress-strain relation and tangent stiffness follow as

$$\pm \mathrm{Z}\ \frac{\alpha}{J^{5/3}}(\mathbf{B} - \frac{1}{3} I_1 \mathbf{I}) + K(J-1)\mathbf{I}, \tag{5}$$

and

$$C_{ijkl} = \frac{\mu}{J^{2/3}}(\delta_{ik}B_{jl} + \delta_{jk}B_{il} - \frac{2}{3}\{\delta_{kl}B_{ij} + \delta_{ij}B_{kl}\}) + \frac{2}{3}\frac{I_1}{3}\delta_{ij}\delta_{kl}) + K\ (2J - 1\ J)\delta_{ij}\delta_{kl}. \tag{6}$$

Here, the initial Young's modulus of the matrix soft material is $E_m = 5MPa$ whereas the stiffer inclusions have initial Young's modulus of $E_i = 50MPa$. Both materials are assumed to have Poisson's ratio $\nu_m = \nu_i = 0.495$ to approximate the incompressibility of rubber-like material. The density of both matrix and inclusion materials is assumed to be $\rho = 1500kg/m^3$. The initial transverse speed of sound in the matrix material is $c_{t0} = \sqrt{\alpha_m / \rho} = 33.4m/s$, and the corresponding value in the inclusions is $c_{t0}' = \sqrt{\alpha_i / \rho} = 105.6m/s$, where $\alpha_{m,i} = E_{m,i} / 2(1+\nu_{m,i})$ is the initial shear modulus of matrix and inclusion material respectively.

2.3 Cohesive interaction

The interaction between two composite fibrils is simulated by a traction-separation relation. In this thesis, we use the bilinear law for simplicity but the qualitative nature of the results depends weakly on the specific form of the cohesive law. The two-dimensional bilinear cohesive law is defined by[47], [48]

$$T_{n,s} = \begin{cases} K_{n,s}\text{¢}_{n,s}, & \text{¢} \le \text{¢}_c \\ K_{n,s}\dfrac{\text{¢} - \text{¢}_f}{\text{¢}_c - \text{¢}_f}, & \text{¢}_c \le \text{¢} \le \text{¢}_f \\ 0, & \text{¢} \ge \text{¢}_f \end{cases}. \tag{7}$$

where $T_{n,s}$, $K_{n,s}$, $\text{¢}_{n,s}$ is the normal or tangent traction, stiffness and separation respectively. ¢ is the magnitude of total separation given by $\text{¢} = \sqrt{\text{¢}_n^{\,2} + \text{¢}_s^{\,2}}$. ¢_c and ¢_f determine the damage initialization and complete failure respectively (Fig. 4).

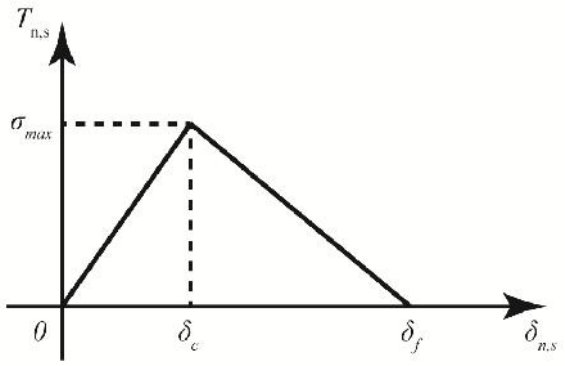

Fig. 4 Bilinear cohesive law of inter-fibril interaction.

The parameters of cohesive law between two fibrils are calculated by assuming an equivalent cohesive material[10], [49] with Young's modulus of $E_{coh} = 1kPa$, Poisson's ratio $\neg_{coh} = 0.495$, and initial thickness $t_{coh} = 1\ll m$. Then we have $\ll_{coh} = E_{coh} / 2(1+\neg_{coh})$, $K_n = E_{coh} t_{op} / t_{coh}$ and $K_s = \ll_{coh} t / t_{coh}$, where t_{op} is the out-of-plane thickness of unit cell. The following characteristic displacements $¢_c = 5\ll m$ and $¢_f = 10\ll m$ are used to determine the damage behavior of cohesive law (Fig. 4). These values are used to represent a weak sacrificial glue layer. From a computational perspective, the tangential stiffness matrix of the interface, which is negative during the softening regime, is added to the stiffness matrix of the composite fibrils to form the global stiffness matrix of the system.

2.4 Wave propagation

The equations of motion are given by

$$\frac{\partial \boldsymbol{\sigma}}{\partial \mathbf{x}} = \rho \frac{\partial^2 \mathbf{u}}{\partial t^2}, \tag{8}$$

in absence of body force, where $\boldsymbol{\sigma}$ is the Cauchy stress and ρ is the density which varies for different material in composite.

The propagation of elastic wave in periodic composites may be analyzed by Bloch's theorem[50] and further developed in the following way[51]. We start by decomposing the solution as

$$\mathbf{u(X,}t\mathbf{)} = \mathbf{U(X)}e^{-iwt}, \tag{9}$$

where $\mathbf{U(X)}$ is a complex valued function of $\mathbf{X}$.

Accordingly we also have the following decomposition for stress

$$\pm(\mathbf{X},t) = \mathrm{p}(\mathbf{X})e^{-iwt}. \tag{10}$$

Eq. (8) now becomes

$$\frac{\partial \mathrm{p}}{\partial \mathbf{x}} = \rho\mu^2\mathbf{U}. \tag{11}$$

Due to periodicity, the displacement is constrained by

$$\mathbf{U(X)} = \mathbf{U(X+L)}e^{-i\mathbf{kL}}. \tag{12}$$

where $\mathbf{L}$ is the vector connecting equivalent points in periodic structure, $\mathbf{k}$ is the wave vector contain the information of wave length and direction.

Similarly, the stress also satisfies

$$\mathrm{p}(\mathbf{X}) = \mathrm{p}(\mathbf{X+L})e^{-i\mathbf{kL}}. \tag{13}$$

Decomposing the displacement field into real and imaginary parts,

$$\mathbf{U(X)} = \mathbf{U}^{\mathrm{Re}}\mathbf{(X)} + i\mathbf{U}^{\mathrm{Im}}\mathbf{(X)}. \tag{14}$$

The displacement constraint becomes

$$\mathbf{U}^{\mathrm{Re}}\mathbf{(X)} = \mathbf{U}^{\mathrm{Re}}(\mathbf{X}+\mathbf{L})\cos(\mathbf{kL}) + \mathbf{U}^{\mathrm{Im}}(\mathbf{X}+\mathbf{L})\sin(\mathbf{kL}). \tag{15}$$

$$\mathbf{U}^{\mathrm{Im}}(\mathbf{X}) = \mathbf{U}^{\mathrm{Im}}(\mathbf{X}+\mathbf{L})\cos(\mathbf{kL}) - \mathbf{U}^{\mathrm{Re}}(\mathbf{X}+\mathbf{L})\sin(\mathbf{kL}). \tag{16}$$

The periodic boundary condition may thus be expressed in matrix form as

$$\mathbf{u} = \begin{Bmatrix} \mathbf{u}_i^{\mathrm{Re}} \\ \mathbf{u}_1^{\mathrm{Re}} \\ \mathbf{u}_2^{\mathrm{Re}} \\ \mathbf{u}_i^{\mathrm{Im}} \\ \mathbf{u}_1^{\mathrm{Im}} \\ \mathbf{u}_2^{\mathrm{Im}} \end{Bmatrix} = \mathbf{Q} \begin{Bmatrix} \mathbf{u}_i^{\mathrm{Re}} \\ \mathbf{u}_2^{\mathrm{Re}} \\ \mathbf{u}_i^{\mathrm{Im}} \\ \mathbf{u}_2^{\mathrm{Im}} \end{Bmatrix}, \text{ where } \mathbf{Q} = \begin{bmatrix} \mathbf{I} & \mathbf{0} & \mathbf{0} & \mathbf{0} \\ \mathbf{0} & \mathbf{C} & \mathbf{0} & \mathbf{S} \\ \mathbf{0} & \mathbf{I} & \mathbf{0} & \mathbf{0} \\ \mathbf{0} & \mathbf{0} & \mathbf{I} & \mathbf{0} \\ \mathbf{0} & \mathbf{-S} & \mathbf{0} & \mathbf{C} \\ \mathbf{0} & \mathbf{0} & \mathbf{0} & \mathbf{I} \end{bmatrix}. \tag{17}$$

Upper scripts of displacement denote the real or imaginary part and lower script i denotes the internal nodes, 1 and 2 denote the corresponding equivalent node pairs. **C** and **S** are corresponding cosine and sine values in Eq. (15) and Eq. (16) in terms of $\mathbf{k}$ and $\mathbf{L}$.

The wave vector is chosen from the first Brillouin zone in reciprocal lattice for the representative unit cell as shown in Fig. 3. The reciprocal lattice is defined by base vectors $\mathbf{A}_1$ and $\mathbf{A}_2$ and

$$\mathbf{A}_1 = 2® \frac{\mathbf{a}_2 \times \mathbf{e}}{a}, \quad \mathbf{A}_2 = 2® \frac{\mathbf{e} \times \mathbf{a}_1}{a}, \tag{18}$$

where $\mathbf{a}_1$, $\mathbf{a}_2$ are base vector in direct lattice (Fig. 3), $a = \|\mathbf{a}_1 \times \mathbf{a}_2\|$ and $\mathbf{e} = (\mathbf{a}_1 \times \mathbf{a}_2)/a$ so that

$$\mathbf{A}_i \mathbf{a}_j = 2®¢_{ij} \tag{19}$$

It is suggested in the literature that the band gap information may be obtained by surfing only the points along boundaries of this zone[52]. While this is not rigorously proven, we adopt the same procedure in the current paper.

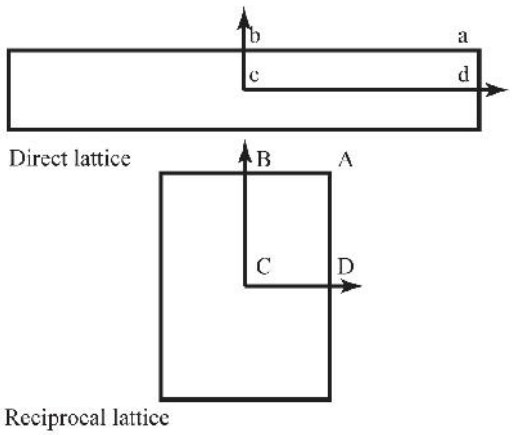

Fig. 5 First Brillouin zone of periodic composite fibril unit cell.

The wave propagation response may then be analyzed by solving the eigenvalue problem of

$$\bar{\mathbf{K}} - \mu^2 \bar{\mathbf{M}} = \mathbf{0}, \tag{20}$$

where $\bar{\mathbf{K}} = \mathbf{Q}^T \begin{bmatrix} \mathbf{K} & \mathbf{0} \\ \mathbf{0} & \mathbf{K} \end{bmatrix} \mathbf{Q}$, $\bar{\mathbf{M}} = \mathbf{Q}^T \begin{bmatrix} \mathbf{M} & \mathbf{0} \\ \mathbf{0} & \mathbf{M} \end{bmatrix} \mathbf{Q}$.

The sub-matrices $\mathbf{K}$ and $\mathbf{M}$ are the stiffness and mass matrix generated from the standard finite element non-linear analysis at different stretch level. The meshes for imaginary and real parts are same which enable us to solve two problems connected by the periodic boundary condition. The solutions of μ are double eigenvalues and give the eigen-frequencies of wave propagating within the elastic material.

We implemented the above framework in an in-house code developed for modeling nonlinear hyperelastic materials and eigenvalue analysis.

2.5 Loading condition

To investigate the deformation pattern, one end of fibirl is stretched at a constant rate along the longitudinal direction to represent displacement controlled loading while the other end is fixed. Both plane stain and plane stress cases are modeled to bound the limits of deformation in finite thickness case. In 3D plate models, we clamp two opposite faces for which one face is kept fixed and the other is stretched in the same manner as in the 2D case. In all cases, the stretching rate is small enough to ensure quasi-static loading.

For band gap structure, we consider uniaxial stretch applied to the infinite periodic composite solid parallel to the layering direction (i.e. horizontally in this case). In order to represent this on the unit cell scale, we apply displacement constraint on upper and lower boundaries and impose prescribed displacement on left and right boundaries. Thus the displacement field in the unit cell is given by:

$$\mathbf{u} = \begin{Bmatrix} \mathbf{u}_U \\ \mathbf{u}_L \\ \mathbf{u}_0 \end{Bmatrix} = \begin{bmatrix} \mathbf{I} & \mathbf{0} \\ \mathbf{I} & \mathbf{0} \\ \mathbf{0} & \mathbf{I} \end{bmatrix} \begin{Bmatrix} \mathbf{u}_U \\ \mathbf{u}_0 \end{Bmatrix} = \mathbf{T}\hat{\mathbf{u}}, \tag{21}$$

where $\mathbf{u}_U$ and $\mathbf{u}_L$ are the displacement vectors of upper and lower boundaries, $\mathbf{u}_0$ is the displacement vector for the interior points and points on the lateral boundaries.

Using the transformation matrices in Eq. (21), the original problem $\mathbf{Ku} = \mathbf{f}$ becomes

$$\hat{\mathbf{K}}\hat{\mathbf{u}} = \hat{\mathbf{f}}, \tag{22}$$

where $\hat{\mathbf{K}} = \mathbf{T}^T\mathbf{K}\mathbf{T}$, $\hat{\mathbf{f}} = \mathbf{T}^T\mathbf{f}$, $\mathbf{K}$ and $\mathbf{f}$ are the stiffness matrix and external force computed from finite element analysis.

CHAPTER 3

MULTI-DIMENSIONAL COMPOSITE DEFORMATION PATTERNS

3.1 1D fibrils

If a homogenous elastomeric fibril is stretched, its length increases and width decreases due to the positive Poisson's effect (Fig. 6a). However, if the fibril is reinforced with staggered inclusions as shown in Fig 1a, it develops a corrugation pattern under stretching. For example, for a modulus ratio r = 30 and spacing s = 40 «m, the fibril deforms periodically in the direction normal to its axis (Fig. 6b). For an elongation of 100 «m (i.e. a stretch value of 1.1) in the plane stress case, the amplitude of corrugation is 6.97 «m (23% of the fibril depth). The corrugation amplitude A is defined as the difference between peak and valley along one side of composite fibril.

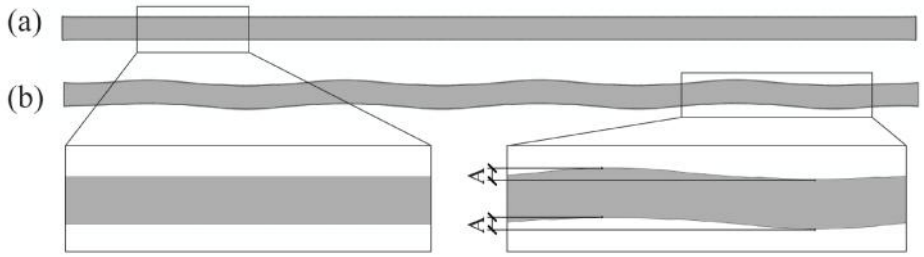

Fig. 6 Deformations of (a) Homogeneous fibril and (b) heterogeneous composite fibril with polymeric inclusions, corrugations develop in plane stress case of the composite fibril. Results are shown for stretch value of 1.10.

Figure 7 shows the evolution of corrugation amplitude as a function of stretch for both the plane strain (a) and plane stress (b) cases. Initial deformation is smooth along longitudinal axis (Fig. 7, stretch = 1.02). As stretching continues, the inclusions starts to bend and corrugation amplitude increases rapidly (Fig. 7, stretch = 1.10). In the limit of large stretch (>1.30) most of the deformation concentrates in the matrix material and axial deformations of the elastomer becomes dominant over the bending deformation (Fig. 7 stretch = 1.30). This leads to a reduction in the rate of the growth of the corrugation. The corrugations rate is initially high (up to stretch value ~ 1.1). After that, the growth rate decreases and eventually saturates. The plane stress case shows systematically higher corrugation values (for the same value of stretch) and lower Von-Mises stresses than the plane strain case.

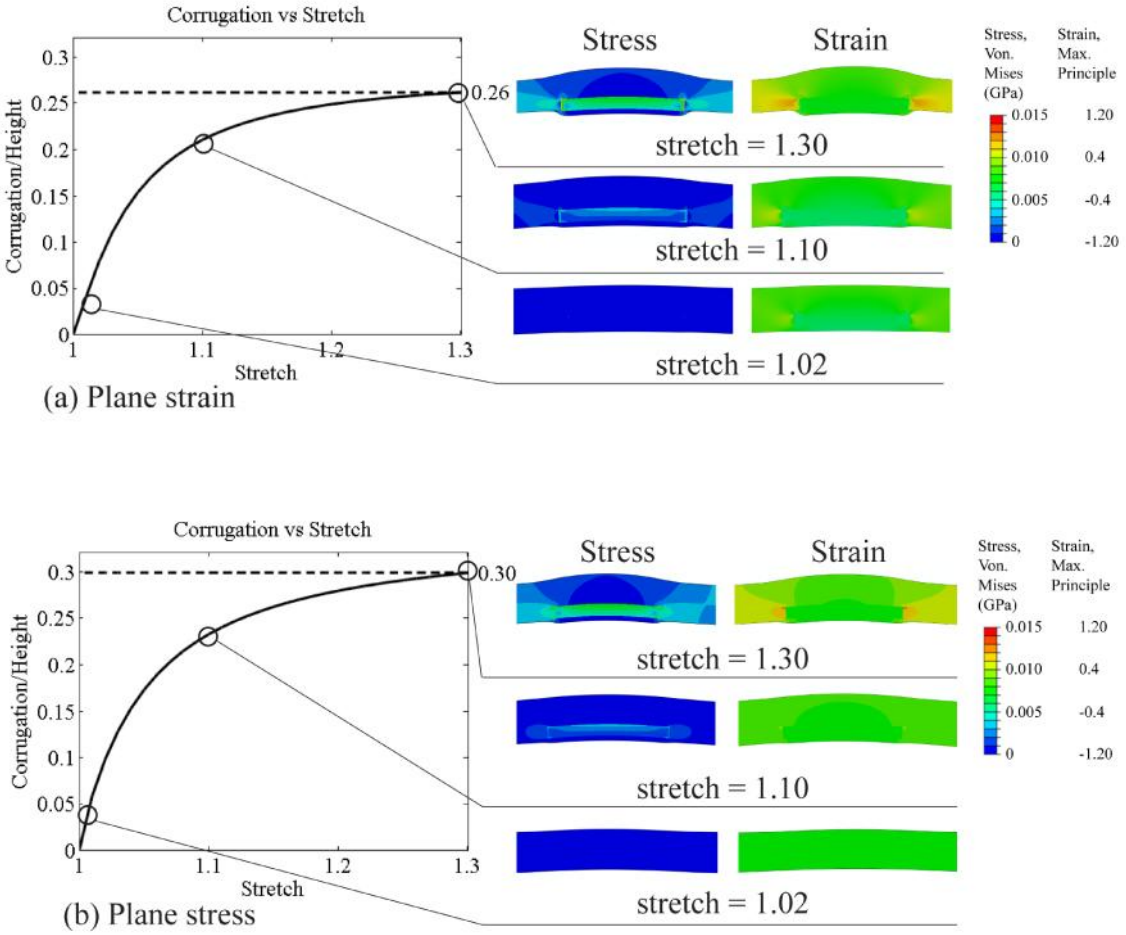

Fig. 7 Corrugation development as a function of stretch. Successive plots show the deformed shape of the fibril when stretch is 1.02, 1.1 and 1.3 in (a) plane strain and (b) plane stress cases.

The development of corrugation under global tensile loading may be explained using the transformation rule for composites. Static equilibrium for the unit cell shown in Fig. 7 requires that applied tension load at one end is balanced by an equal and opposite collinear load at the other end. Thus the two equilibrating forces are acting along the axis of the fibril. However, due to the presence of inclusions with a different modulus, the center of area of the mineralized section does not coincide with the geometric center. The center of area of a heterogeneous

section is computed by transforming the section into an equivalent homogenous one. This is done by multiplying the area of the stiffer inclusion by the modulus ratio to transform it into an equivalent area of the matrix material. As a results the center of area of the homogenized section is shifted towards the location of the inclusion (see Fig. 7, stretch = 1.10, 1.30). While the loading is uniformly applied at the fibril ends, the shifting in the center of area in the interior section causes eccentricities that follow the periodic inclusion patterns. Accordingly internal moments develop and periodic bending deformation is triggered. As the corrugation amplitude increases, the center of area of the equivalent homogenous section is pushed towards the fibril axis and the eccentricity is gradually reduced. This also explains the decrease in the rate of growth of corrugation with increasing stretch (Fig. 7). Throughout the stretch process, the stress level of matrix field is below the ultimate strength of rubber at $0.015GPa$.

3.1.1 Effect of spacing and material contrast

To investigate the effect of material contrast we consider different values of moduli ratio *r* equal to 1, 3, 6, 10, 30 and 50 respectively. In each case, we examine the influence of platelet spacing by modeling different values $s = 0\mu m, 20\mu m, 40\mu m, 60\mu m, 80\mu m$. For generalization, spacing and corrugation are normalized by fibril height to produce dimensionless values. Contours for maximum corrugation at stretch = 1.3 are shown as a function of stiffness ratio and normalized spacing in Figures 8a and 8b. On one hand, for a fixed value of *s*, the corrugation amplitude increases as the modulus ratio *r* increases but eventually levels off. On the other hand, for a fixed

value of r , increasing the spacing has only a weak effect on the corrugation amplitude but it does control the corrugation wavelength (not shown here). These results may be explained as follows.

As the modulus ratio increases, the equivalent area of the inclusion becomes larger leading to a higher eccentricity of the center of area and accordingly larger bending deformation. However, if the inclusion modulus is high enough, the inclusion becomes harder to bend. In this case the fibril accommodates the external loading through the stretching of the elastomeric matrix rather than increasing the bending amplitude. The larger the spacing between the inclusions, the larger the volume of the soft matrix that is capable of stretching freely and thus the corrugation amplitude saturates at a lower value of r than in the case of smaller spacing.

The weak dependence of corrugation amplitude on the inclusion spacing at a fixed value of moduli ratio is due to the fact that the spacing does not contribute to the eccentricity of the center of area of the transformed section, the primary source of bending deformation. However, the soft matrix between the inclusions must rotate and elongate to ensure the continuity of the deformed curve of the corrugated beam. Since stretching dominates over bending in the background polymer matrix, the slight rotation contributes to only a slight increase in the deflection in the reinforced portions of the fiber.

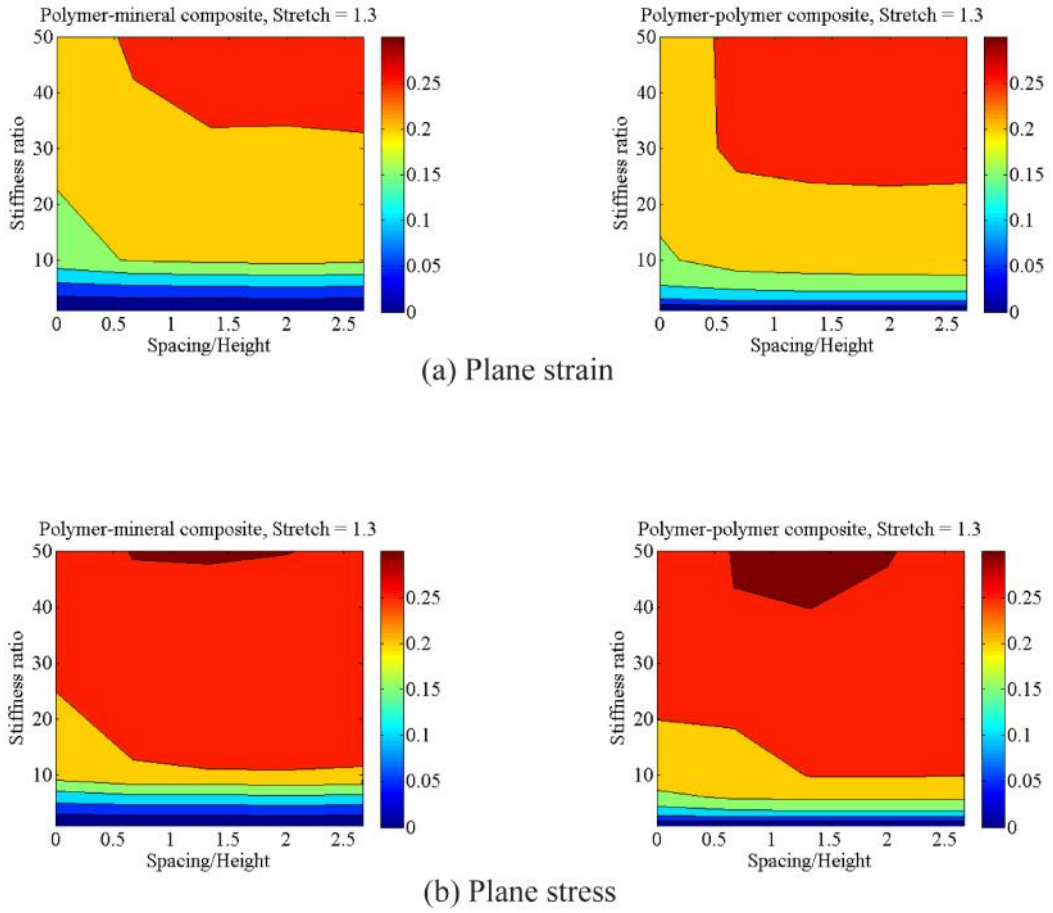

Fig. 8 Effect of elastic moduli ratio and inclusion spacing on normalized corrugation amplitude (corrugation/height): polymer-polymer model of matrix material with initial Young's modulus E_m=0.005GPa, inclusion material modeled as hyperelastic material; polymer-mineral model of matrix material with initial Young's modulus E_m=1GPa, inclusion material modeled as elastic material .The results are presented for both (a) plane strain and (b) plane stress cases.

3.1.2 Effect of eccentricity and inclusion aspect ratio

To investigate the effect of eccentricity and inclusion aspect ratio, we examine different values of c and L_i / t on polymer-polymer composite model. We choose $2c = 3\text{«}m, 6\text{«}m, 9\text{«}m$ and vary the aspect ratio between 2 and 12. The results are summarized in Fig. 9.

Lower aspect ratio generates smaller corrugation while increasing the inclusion eccentricity leads to larger corrugation. These observations may be explained as follows. For a fixed inclusion thickness *t*, the lower the aspect ratio corresponds to shorter length and hence higher inclusion stiffness. As a result, the bending resistance of the inclusion increases, and the wavelength of the corrugation decreases. The deformation is primarily accommodated by elongation in the elastomeric matrix. On the other hand, if the inclusion eccentricity increases, the center of area of the transformed section is pushed further away from the fibril axis. As a result the internal bending moment increases and so does the corrugation amplitude.

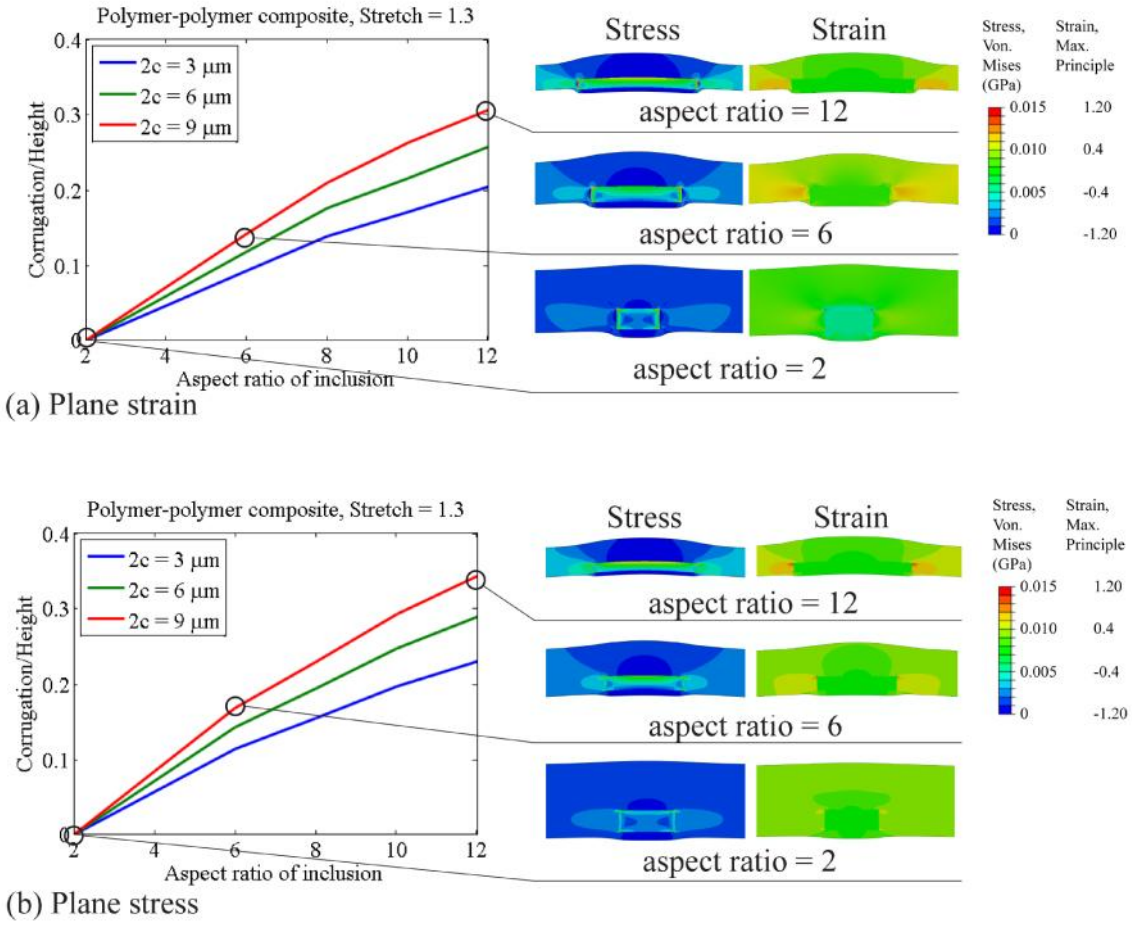

Fig. 9 Effect of inclusion aspect ratio and eccentricity on normalized corrugation amplitude (corrugation/height) of polymer-polymer model in (a) plane strain and (b) plane stress cases, results are shown corresponding to final stretch = 1.3, , L = 1000µm, h = 30µm, t = 7.5µm, s = 40µm, moduli ratio r = 100.

3.1.3 Mesh Sensitivity Analysis

We conduct a numerical experiment to analyze the effect of mesh refinement on the results of corrugation amplitude. The benchmark problem we study is the corrugation of single fibril under stretch in both plane stress and plane strain cases. The material and geometric properties are the

same as in the model used to produce the results shown in Fig. 7. The corrugation amplitudes at stretch values 1.10 and 1.30 are illustrated in Fig. 10.

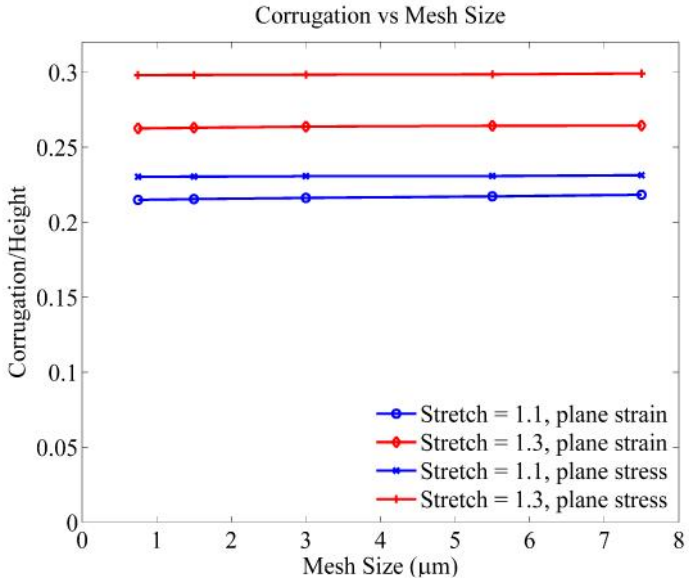

Fig. 10 Mesh sensitivity effects of single fibril under stretch.

Figure 10 suggests that the corrugation amplitude converges in the continuum limit (i.e. as the mesh element size approaches zero). For the range of element sizes considered here, the absolute magnitude of corrugation varies only by $0.01 \ll m$ between the coarsest and finest meshes. We choose the element size to be $1 \ll m$ in the simulations conducted in this study in balance of cost and precision.

3.1.4 Effect of inclusion corners

Stretching the composite fibril causes stress concentration near the edges of the inclusions when inclusions have sharp corners (Fig. 11a). The maximum value of hydrostatic stress (positive when compression) within the matrix material occur near the inclusion/matrix interface. For the case shown in Fig. B11a, this value is $0.012 GPa$ in plane strain case and $0.0024 GPa$ in plane stress case. The former value may lead to cavitation instabilities. To reduce the stress

concentration in the plane strain case, we model a system in which the inclusions have rounded corners (Fig. 11b). The hydrostatic stress in the matrix is reduced as a result from 0.012 *GPa* to $0.0047GPa$. Thus, susceptibility to fracture and cavitation may be greatly reduced by tailoring the geometry of the elongated inclusion in our system. We have found that imperfect bonding between the inclusion and the matrix material, modeled by a traction-separation law, may further reduce the stress concentration by allowing for some local deformation without complete separation. This issue demands further investigation.

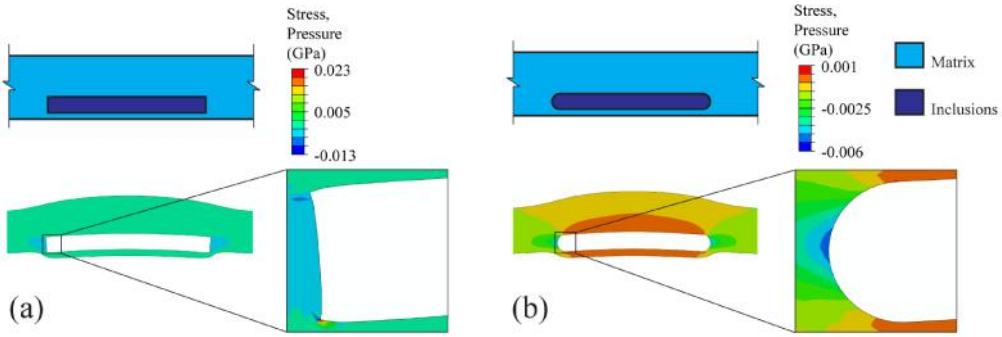

Fig. 11: Local hydrostatic pressure distribution in matrix near perfectly bonded inclusion in the plane strain case: (a) Inclusion with sharp corner; (b) Inclusion with rounded corner: stretch = 1.3, fibril dimension L = 1000µm, h = 30µm, inclusion dimension L_i = 75µm, t = 7.5µm, spacing s = 40µm, array distance c = 4.5µm , moduli ratio r = 30.

3.2 2D Membranes

Corrugation patterns observed above may be extended to higher dimensions. As a starting point, we consider two composite fibrils that are glued along their longer edge using a weak adhesive described in Chapter 3. The use of an adhesive material along the interface may be necessary for initial assembly of the fibrils and the integrity of the manufacturing process. Also, the adhesive

helps in sealing the inter-fibril openings at the early stages of loading that will otherwise open right away due to fibril contraction in the transverse direction (due to positive Poisson's effect). Three cases with different inclusion distributions are investigated below and are shown schematically in Fig. 12. We show our results for both the plane stress and plane strain cases in Fig 13.

In the first case, the distribution of inclusions in the two composite fibrils is symmetric about the glue line (Fig. 12a). Several contact regions develop. In between these regions, the fibril moves away from one another. If the adhesive is weak enough it will resist the fibril separation for a brief period $¢_f$ and then break leading to the formation of channels as shown in Fig. 13.

The existence of the adhesive ensures that the contact regions remain closed. For a stretch of 1.1 the maximum opening at the channel location is $12.87«m$ in plane strain case and $13.88«m$ in plane stress. Recalling that the corrugation amplitude is dependent on the stretch (Fig. 7), and since both the matrix and the inclusions are operating within their elastic regime, we argue that the procedure introduced here may be a viable tool for constructing membranes with tunable channel sizes. We discuss the implications of this in Chapter 5.

In the second case, the two fibrils have identical distribution of inclusions (Fig. 12b). Upon stretching, the two fibrils conform to one another and interlock (Fig. 13). The adhesive strength is adequate to keep the crevices size under maximum elongation $¢_f$ and prevent the fibrils from

separation. The oblique orientation of the sealed crevices, however, may be useful in generating certain band gap patterns. This will be explored elsewhere.

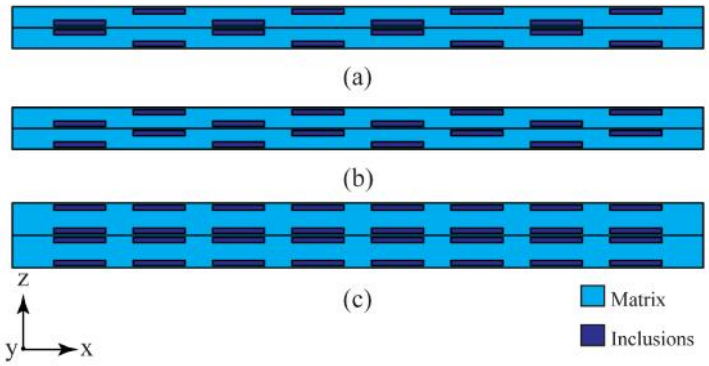

Fig. 12 (a) Symmetric, (b) identical and (c) non-staggered distribution of inclusions.

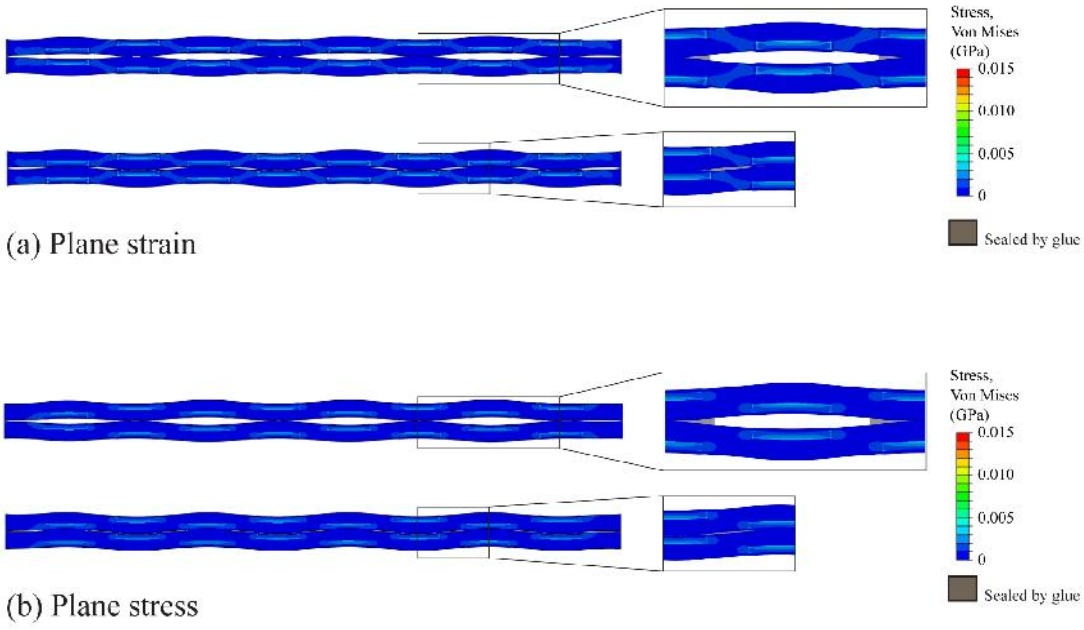

Fig. 13 Deformation of two composite fibrils with symmetric and identical staggered distribution of inclusions in (a) plane strain and (b) plane stress cases: 1.1 Stretch on polymer-polymer materials with matrix initial Young's modulus E_m=0.005GPa, inclusion material modeled as hyperelastic material, composite fibril dimension , L = 1000µm, h = 30µm, inclusion dimension L_i = 75µm, t = 7.5µm, spacing s = 40µm, moduli ratio r = 30.

In the third case, the two fibrils have identical distribution of aligned inclusions as above (Fig. 12c). Within each fibril the inclusions are symmetrically distributed about the fiber axis. Upon stretching, no corrugation will form in either fibril as expected. However, the softer matrix within the spacing between the inclusions contracts laterally more than the stiffened portions (Fig. 14). In plane strain case, since the contraction within the softer regions is larger than the adhesive capacity, the adhesive layer detaches and periodic channels form as shown in Fig. 14a. In plane stress case, as contraction is smaller, weak adhesive ensures that the openings remains completely sealed (Fig. 14b).

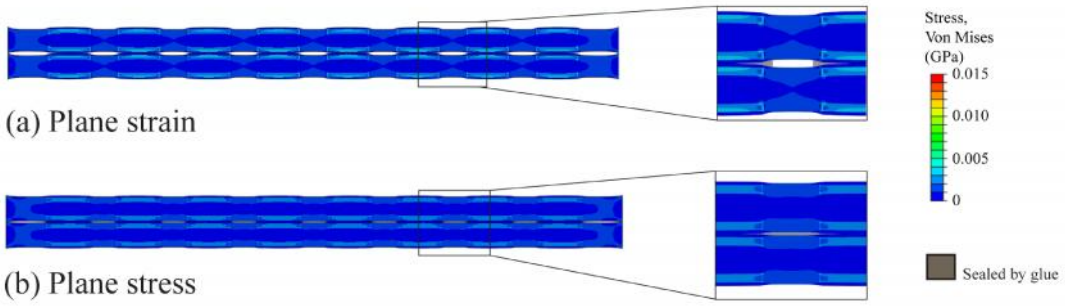

Fig. 14 Deformation of two composite fibrils with non-staggered distribution of inclusions in (a) plane strain and (b) plane stress cases: [array distance c = 12μm, other parameter same as Fig.13].

We note that in all these cases with weak cohesive strength, the channels develop gradually in response to the applied loading. No instability or transition to dynamic crack growth is observed. There are two possible reasons for this. First, the weak interface has a relatively small softening slope and hence the strength degradation occurs gradually. Second, due to the corrugation patterns of the joined fibrils, there is always a closed contact region ahead of the crack tip

(corresponds to fibrils moving towards one another). This local compression stabilizes the channel growth and opening. However, with stronger cohesive strength and steeper softening slope, the interaction between the fibril elastic stiffness and the interfacial stiffness may lead to dynamic instability and a sudden opening of the channels.

3.2.1 Effect of cohesive interfacial strength

The dynamics of channel growth in 2D membranes is controllable by adjusting the strength of the cohesive interface. Here we show some results from our preliminary investigations on the effect of the cohesive interface properties on the dynamics of channel growth. We conduct a series of simulations modeling two composite fibrils with different cohesive interfacial strength T_{ult} and stiffness (Fig. 15a). The results suggest that there exits three distinct regions of channel response depending on the peak cohesive strength. For weak strength (Fig. 15b, $T_{ult} \le 3kPa$), the deformation remains quasistatic, the channel expands gradually (Fig. 16a) and the interfacial openings develop smoothly (Fig. 17a). For higher cohesive strength values (Fig. 15b, $T_{ult} > 30kPa$), the glue never break completely and it continues to seal the interface with no opening development between the two fibrils. For intermediate values of cohesive strength (Fig. 15b, $3kPa < T_{ult} \le 30kPa$), there will be a transient dynamic instability. The inter-fibril channels will open abruptly (Fig. 15b), causing sudden loss of the cohesive traction (Fig.16b) and a jump in the channel growth rate (Fig.17b).

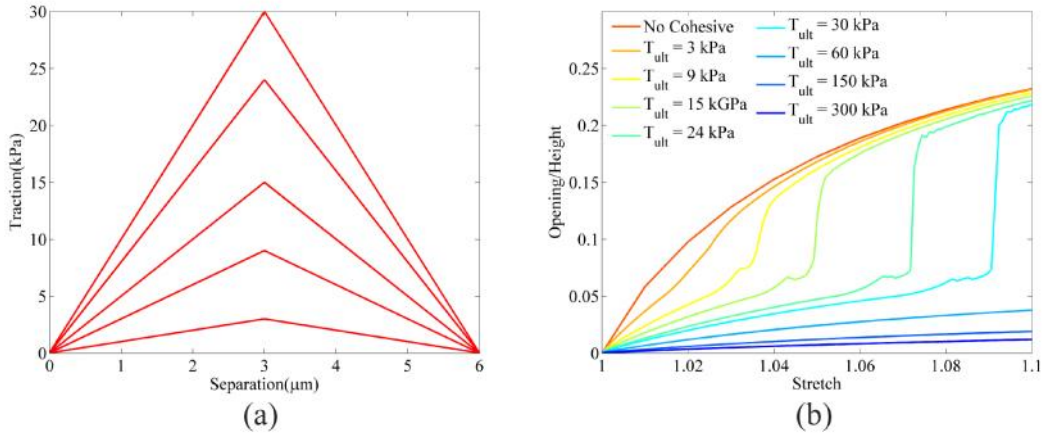

Fig. 15 (a) Cohesive laws with different cohesive strength (b) Effect of cohesive strength on corrugation development.

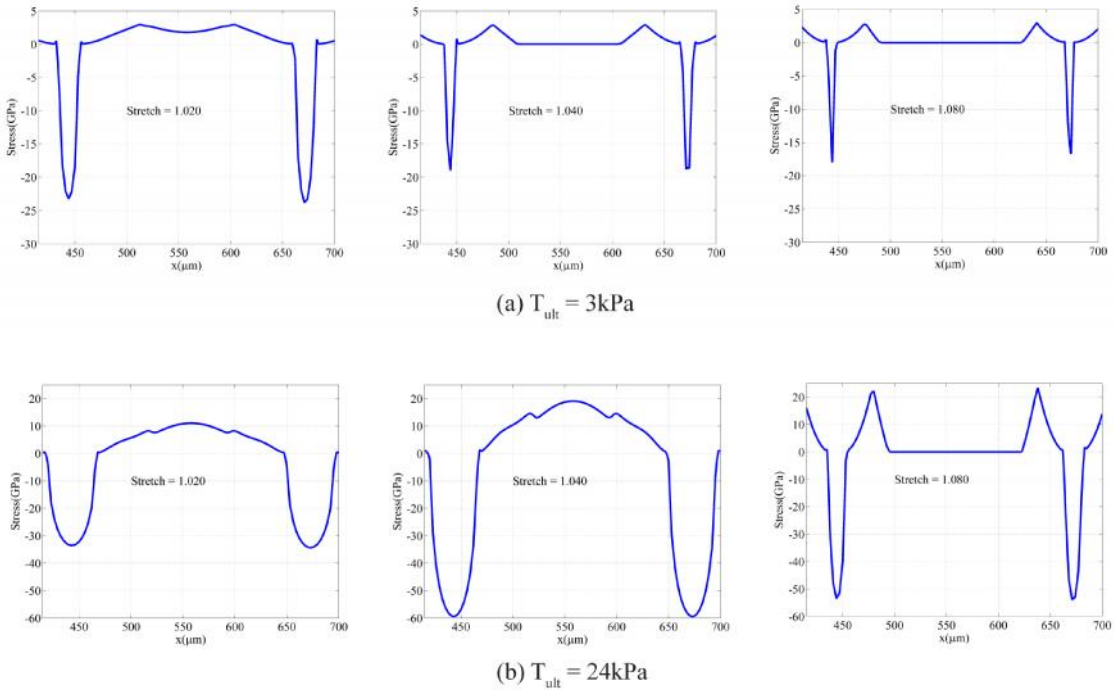

Fig. 16 Cohesive stress (positive for tension and negative for compression) distribution along one opening position

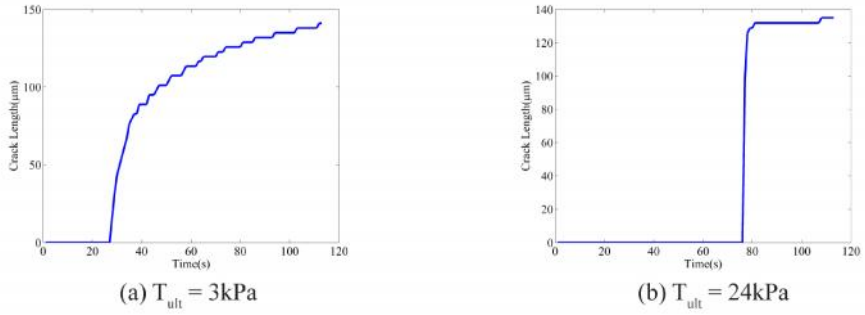

Fig. 17 Crack length (Opening with detachment of cohesive law)

The interaction between the elastic stiffness of the fibrils and the interfacial properties lead to a rich behavior ranging from quasistatic deformation to transient dynamics instability. Our preliminary investigation suggests that it may not be adequate to describe the interfacial response by a single parameter such as fracture energy. Additional parameters such as peak cohesive strength and softening slope may play an important role as shown above. In particular a full characterization of the cohesive behavior may be required to investigate the transition from ductile to brittle interfacial response (and correspondingly the switch between stable channel growth and dynamic channel growth). Detailed study of this topic will be a focus of further investigations.

3.3 3D plates

Tension induced corrugation may be used in designing controllable non-planar geometries from planar sheets of material. Recall from Fig. 2 that the 3D construction is essentially a laminated plate in which the reinforcing inclusions exist in the second and fourth layers. Here we consider the case of a mineralized polymer composite with material properties similar to the collagen

hydroxyapatite composite. The generated corrugation pattern depends critically on the distribution of the stiff inclusions in-plane and through the thickness direction. Three cases are investigated and are shown in Fig. 18 as proof-of-concept. In the first case (Fig. 18a), the inclusions are staggered sheets placed with their longitudinal axis normal to the loading direction. This geometry is developed by extruding composite fibril in the y-direction (See Fig. 1) and the corrugation pattern is alternating valleys and crest regions parallel to the y-axis. In the second case (Fig. 18b), the inclusions are square plates staggered in the thickness direction but are aligned along the x-direction. The corrugation pattern resembles a regular egg-box. In the third case (Fig. 18c), the inclusions are staggered in plane and through thickness. The resulting corrugation pattern is similar to a skewed egg-box. This technique may be further used to develop surfaces of tunable roughness profile that depends on the level of deformation by carefully designing the inclusion pattern. Guttag and Boyce[53] have recently used a similar idea to develop surfaces that get rougher by the application of compressive loading on a reinforced composite.

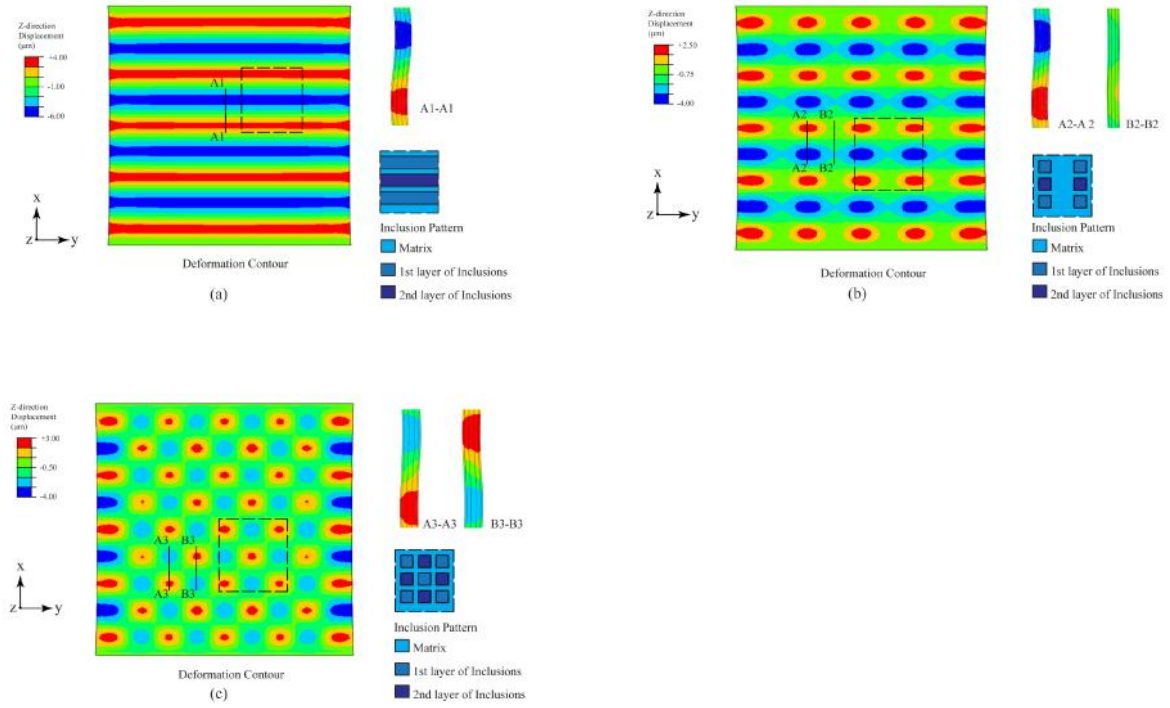

Fig. 18 Inclusion distribution and corrugation patterns in a composite plane: (a) inclusion platelet size = $1000\text{«}m \times 75\text{«}m \times 7.5\text{«}m$, spacing = $32.5\text{«}m$, maximum corrugation = $8.2\text{«}m$ at surface; (b) inclusion size = $75\text{«}m \times 75\text{«}m \times 7.5\text{«}m$, $32.5\text{«}m$ spacing along stretch direction, $140\text{«}m$ spacing perpendicular to stretch direction. Maximum corrugation = $5.4\text{«}m$ at surface; (c) inclusion size = $75\text{«}m \times 75\text{«}m \times 7.5\text{«}m$, $32.5\text{«}m$ spacing in both directions, maximum corrugation = $4.9\text{«}m$ at surface.

CHAPTER 4

BAND GAP STRUCTURE

4.1 Deformation and damage

To investigate the influence of the interfaces, the deformations of both monolithic (i.e. no interfaces) and fibril systems (with interfaces) under uniaxial stretch are simulated and compared.

Two monolithic composites with inclusions that are arranged in (1) symmetrically aligned pattern and (2) staggered pattern serve as a reference group. Compared to the layered system (Fig.3), there are no interfaces in the monolithic case (Fig. 19a, 19b). The monolithic nature of matrix material leads to strong constrain of unit cell deformation which stiffens the overall composite under external load. In case (1), due to the bi-symmetrical geometry distribution of material, the unit cell retains its rectangular shape and the inclusions remain parallel to each other under uniaxial stretch (Fig. 19a). In case (2), the lack of symmetry in the lateral direction leads to changes in the shape of the unit cell. The inclusions, however, remain parallel to each other due to their lower compliance than matrix (Fig. 19b).

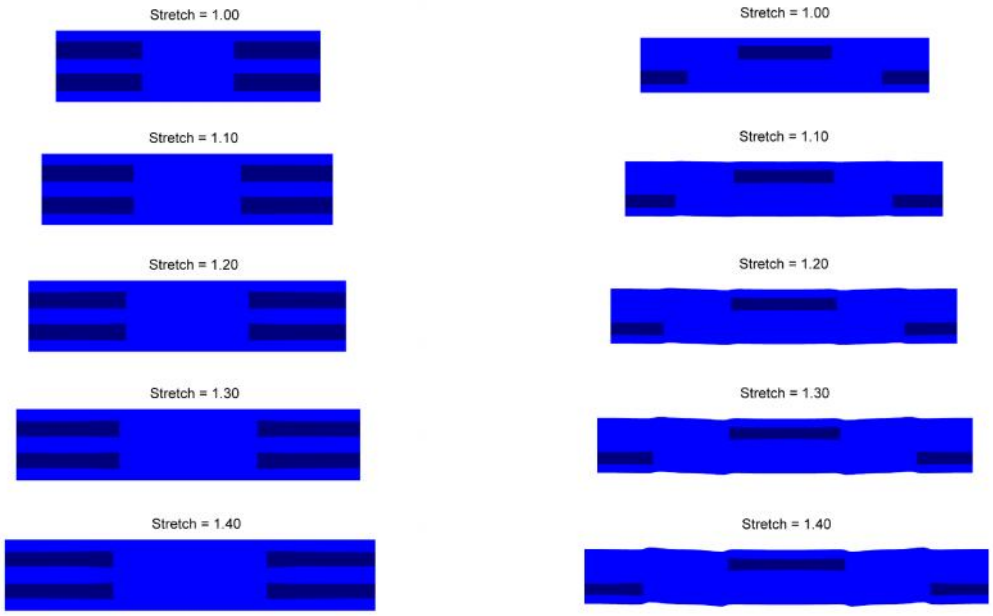

(a) (b)

Fig. 19 Evolution of deformed shape of a unit cell as a function of stretch in (a) monolithic composite with symmetrically aligned inclusion pattern, and (b) monolithic composite with staggered inclusion pattern.

The introduction of interfaces enables a more complex deformation pattern. Each fibril deforms according to the inclusion distribution within matrix material. In the symmetrically aligned case, the transverse deformation of the fibril varies spatially according to the location of the inclusion, and separation develops between each pair of fibrils (Fig. 20a). The fibril is effectively stiffer in the regions where inclusions exist. Accordingly, the fibrils shrink more, in the transverse direction, in regions of the pure matrix material. The cohesive interface start to incur damage after the separation exceeds the critical separation $¢_c = 5«m$. Interfacial channels grow when the transverse separation between two fibrils is beyond the detachment separation $¢_f = 10«m$ of the glue material.

In the case where inclusions are distributed in a staggered pattern, corrugations develop as shown in Fig. 20b, 20c. Composite fibrils interlock with each other in a periodic manner. After the separation exceeds $¢_f$, channels form in an oblique orientation. Those channels undergo an almost rigid body rotation as they grow and as the stretch level increases. Two values of $¢_c$ and $¢_f$ are considered to evaluate the effect of cohesive interface ductility. In the first case, where $¢_c = 5 « m$ and $¢_f = 10 « m$, total separation in the channel regions happens at stretch = 1.30(Fig. 20b). In the second case, where $¢_c = 10 « m$ and $¢_f = 20 « m$, because of the larger ductility of cohesive interface, total separation will not happen even at stretch = 1.40(Fig. 20c). Due to the large elastic compliance of the cohesive interfaces in both cases, the deformation of the fibrils is comparably similar. However, we will see that the band gap is structure is somewhat different in the two cases especially at large stretch.

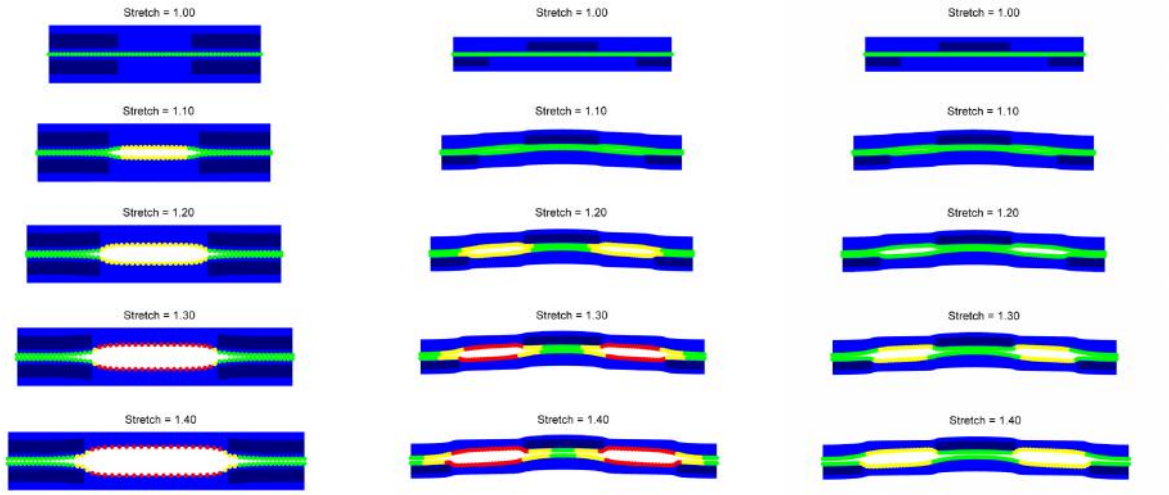

(a) (b) (c)

Fig. 20 Evolution of deformed shape of a unit cell as a function of stretch in (a) layered composite with symmetrically aligned inclusion pattern and sacrificial interface with low interfacial ductility, (b) layered composite with staggered inclusion pattern and sacrificial interface with low interfacial ductility, and (c) layered composite with staggered inclusion pattern and sacrificial interface with high interfacial ductility (high interfacial ductility). Damage state of the interfacial cohesive material is denoted by the color of the points where green corresponds to deformation within elastic region, yellow marks deformation after the damage initialization (i.e. along the softening branch) and red indicates total separation .

4.2 Band gap evolution

By solving the eigenvalue problem Eq. (20), we obtain the dispersion plots shown in Fig. 21 and 22. Here the x-axis denotes the wave vector in reciprocal lattice and y-axis denotes the normalized eigen-frequency $\tilde{f} = fa / C_{t0}$, where $f = \mu / 2®$ is the eigen-frequency, $a = (a_1 + a_2)/2$ is half of the sum of the length and width of the deformed representative unit cell.

The dispersion relation of monolithic matrix material models are given in Fig. 21a and Fig. 21b. We observe that no band gap is generated in the two cases for the specific material contrast and inclusion spacing considered. As stretch level grows up, the eigen-frequencies of the system increase, due to the deformation-induced stiffening of the hyperelastic materials.

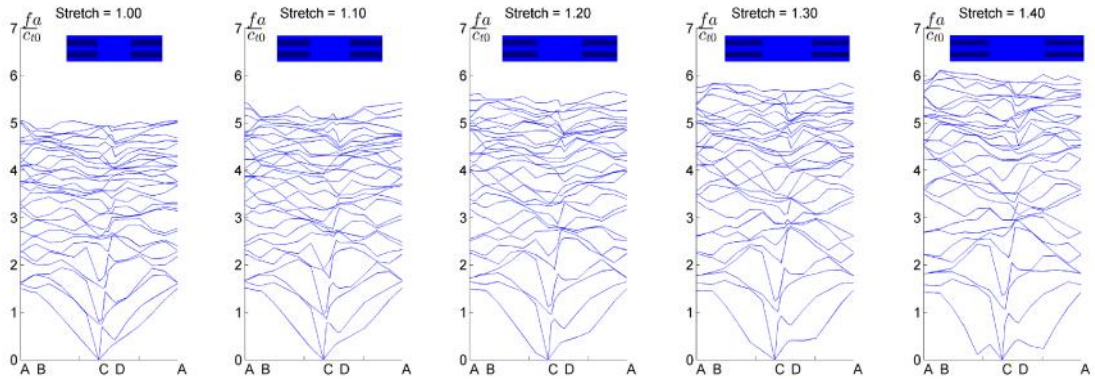

(a)

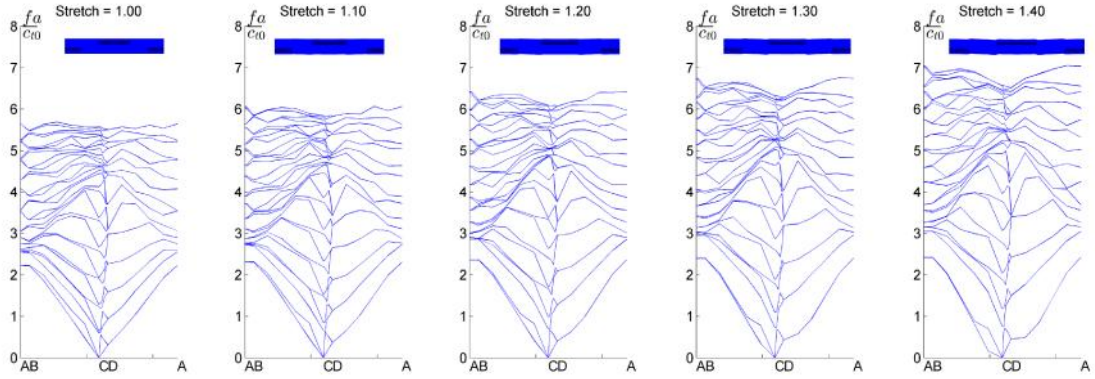

(b)

Fig. 21 Dispersion plots at different stretch levels for monolithic composites with (a) symmetrically aligned inclusion pattern and (b) staggered inclusion pattern. No band gaps exit at any level of stretch.

For the layered composite, the behavior is completely different even for the same inclusion pattern. In the case of the symmetrically aligned inclusions, several band gaps develop at zero stretch (Fig. 22a). Initially, some narrow band gaps exist, mainly at high frequencies ($\tilde{f} > 3$). After the damage of the interface initializes (at stretch = 1.10), some of the original band gaps

vanish and some new band gaps appear at $\tilde{f} < 3$. When the stretch reaches 1.20, higher frequencies are completely barred and a wider band gap exists near $\tilde{f} = 1.5$. As the total separation begins (at stretch = 1.3 and higher), many band gaps form for both high and low frequencies and they tend to increase in width under further stretch.

In the case of staggered inclusion pattern with $¢_c = 5«m$ and $¢_f = 10«m$ (Fig. 22b), fewer band gaps are present initially compared to the symmetrically aligned case. With the onset of total separation in the channel regions (stretch = 1.3 and higher), more band gaps appear. In the case where $¢_c = 10«m$ and $¢_f = 20«m$ (Fig. 22c), total separation in the channel regions does not develop even at the maximum stretch level considered here due to the increased ductility of the cohesive law. Compared with the case of lower interface ductility, thinner and fewer band gaps exist at stretch levels of 1.30 and 1.40. This behavior suggests that interfacial properties play an important role in band gap structure even when the interface is much weaker than the matrix material.

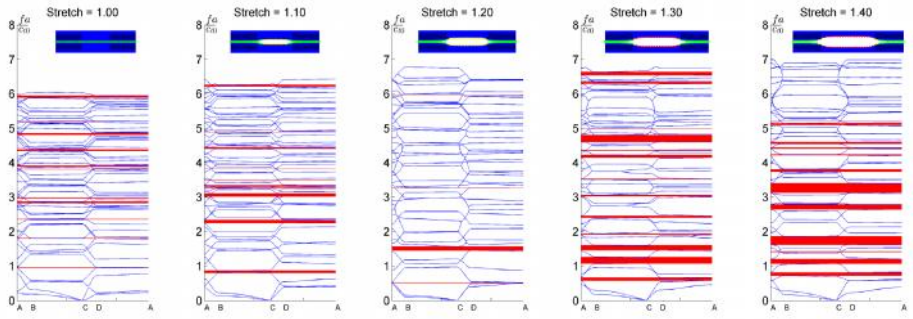

(a)

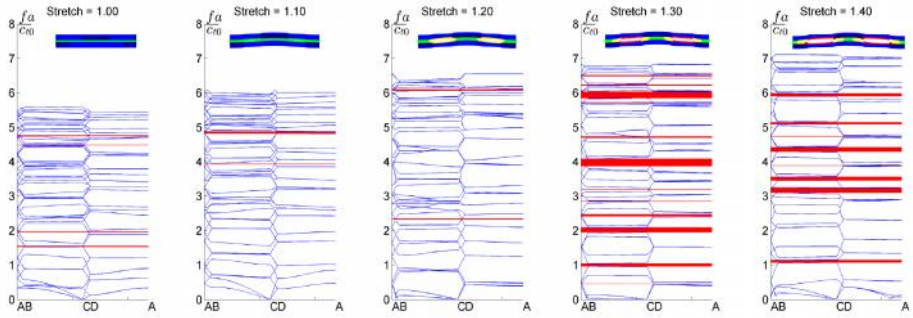

(b)

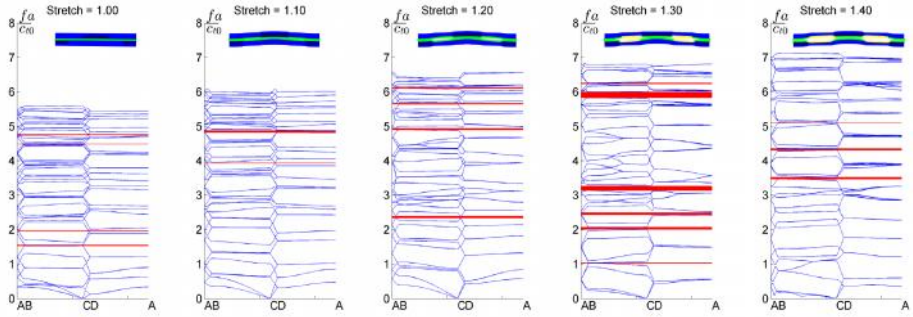

(c)

Fig. 22 Dispersion plots at different stretch levels for layered composites with (a) symmetrically aligned inclusion pattern and sacrificial interface with low interfacial ductility, (b) staggered inclusion pattern and sacrificial interface with low interfacial ductility, and (c) staggered inclusion pattern and sacrificial interface with high interfacial ductility. Damage state of the interfacial cohesive material is denoted by the color of the points where green corresponds to deformation within elastic region, yellow marks deformation after the damage initialization (i.e. along the softening branch) and red indicates total separation .

The evolution pattern of the band gap structure as a function of stretch is summarized in Fig. 23. The band gaps evolve under the competing effects of two processes: (i) deformation induced stiffening of the hyperelastic material that tend to make band gaps move towards higher frequencies, and (ii) deformation induced softening due to damage and localized separation along the sacrificial interface which is also accompanied by changes in local geometry.

In the symmetrically aligned case (Fig. 23a), band gaps initially exist within frequency range $\tilde{f} > 3$. Their widths keep constant and positions shift up before initial damage begins. When the stretch reaches 1.10, most of those initial band gaps vanish and some new band gaps appear at $\tilde{f} \in [3,5]$ but fade away after stretch level of 1.20. At this stage, band gaps are most noticeable for $1 \le \tilde{f} \le 2$. When the total separation within the channels begins after stretch = 1.30, many band gaps show up at both high and low frequencies. In particular, as the stretch level increases, the low frequency band gaps increase in width and number. This rich behavior suggests that sacrificial interfaces may be an effective way in producing multiband gap structures including low frequency band gaps.

In the staggered case (Fig. 23b, 23c), fewer band gaps appear throughout the stretch process. Initial band gaps shift to higher frequencies and vanish after damage begins at stretch = 1.20. New band gaps appear and widen but then vanish between stretch of 1.20 and 1.40. The main difference is that for interfaces with increased ductility (Fig. 23c) no low frequency band gaps ($\tilde{f} < 2$) emerge between stretch levels of 1.25 and 1.4 whereas the composite with reduced

interfacial ductility (Fig.23b) has a band gap there. This is because with increased interfacial ductility, no complete separation within the channels happens and thus the interface is still capable of conducting wave propagation. On the other hand, if complete separation happens, waves have to diffract around the channels. This in turn may lead to band gap formation.

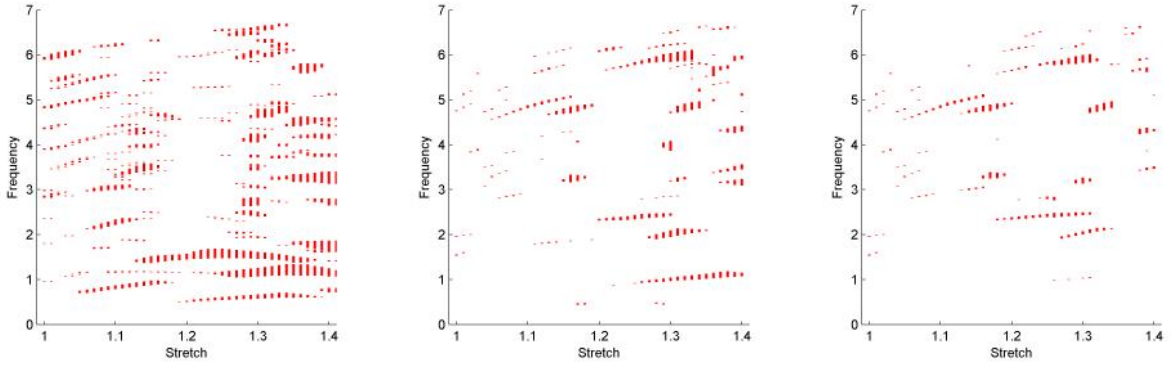

(a) (b) (c)

Fig. 23 Band gap evolution as a function of stretch in layered composites with (a) symmetrically aligned inclusion pattern and sacrificial interface with low interfacial ductility, (b) staggered inclusion pattern and sacrificial interface with low interfacial ductility, and (c) staggered inclusion pattern and sacrificial interface with high interfacial ductility. Complete interfacial separations within the channel regions lead to the emergence of low frequency band gaps (cases a and b) as compared to cases where the interface remains partially damaged (case c).

CHAPTER 5

DISCUSSIONS AND CONCLUSION

In this thesis we present a numerical model for the deformation of a two-phase elastic composite under uniaxial stretch and explore some of its possible design implications. One phase is chosen to be a polymer while the inclusion phase may be either a mineral or another polymer. Such composites are abundant in natural materials such as bone[54]–[56] and sea sponge[57] as well as in engineered materials such as fiber reinforced concrete[58], asphalt concrete[59] and nanofiller reinforced rubber[60]. Extensive studies have been carried out, using homogenization theory, to characterize the effective properties of these composites at the macroscale based on their microstructure[61]–[63]. A point of departure in the current investigation is the use of inclusions of comparable dimensions to the overall composite dimensions and thus the whole composite is analyzed and not just a representative unit cell. This opens new opportunities for identifying unexpected deformation patterns that may be suppressed in the homogenized representation.

The development of corrugation in a single composite fibril may be explained on the basis of the transformation theory of composites. While the external load is concentric, the inclusions change the effective stiffness along the fibril length leading to the development of internal eccentricities and thus bending deformation. The resulting corrugations increase with the inclusion stiffness

and eccentricity from the fibril axis. The corrugation amplitude also weakly depends on the inclusion spacing.

While corrugations in a single fibril may be of little interest in its own, the potential for exploiting this phenomenon in 2D and 3D may lead to several interesting applications. For example, we show that by assembling composite fibers with different inclusion distributions in the plane, the stretch-induced corrugation in each individual fibril may collectively lead to the formation of channels of different shapes and orientation within the composite sheet. The size of these channels is a function of the applied stretch and hence is tunable. The elasticity of the constituent materials ensures that the deformations, including the opening of the channels, is reversible and hence may be reproduced repeatedly. In this particular case, effect of fatigue response must be considered. This is beyond the scope of the current paper.

The interfacial glue used in constructing 2D membranes from 1D fibrils is modeled using cohesive elements. This modeling assumption may be justified by the confinement of separation between the fibrils to the well-defined interfacial region and the small thickness of the glue layer relative to the dimensions of the joined fibrils. In case of thicker interfaces, or if distributed damage is expected to occur outside the interfacial region, a more refined model may be required. For example, the glue may be modeled explicitly as a layer with its own bulk finite elements or alternatively the membrane response may be enriched by a continuum damage model. However, our simulations suggest that the fibrils remain within their elastic limits even after interfacial

separation and channel opening. This may support the adequacy of the cohesive element implementation for the current purposes. Furthermore, this suggests that the fibril deformation may be reversed upon reducing the stretch and that the channels may be closed if desired (since the fibrils remain elastic). The closure of the channels may provide an opportunity for the self-healing of the glue layer if its chemistry allows. An example of such self-healing interfaces may be polymers with hindered urea bonds[64]. This facilitates the full reversibility of the process.

It was previously shown that it is possible to change the void patterns in an elastomer through compressive buckling leading to tunable band gaps and auxetic response[65]. The current approach may provide additional flexibility and more controllability over this process. In particular the void shapes and sizes in the current case are tuned by the amplitude of stretch. Tension-like loading is more easily controlled than instabilities induced by buckling. Moreover, tension loading will not induce undesired out of plane instabilities that may sometimes occur under compressive loading. The voids are not introduced a priori in the elastomer but they develop and are patterned following the inclusion distribution. This may be a more flexible way, from a manufacturing perspective, to generate holes in the polymer matrix, than to precisely machine these holes from the beginning.

Developing complex 3D geometries, especially at nano and micro scale, is a topic of immense interests in a variety of fields[16]–[19]. The recent advances in 3D printing[20] as well as in

origami engineering[66], [67] have opened new opportunities in that realm that were not thought of a few years back. Here we show that by designing the distribution of inclusions in a polymer laminated plate, it is possible to create pop-ups and valleys in the plate with controllable pattern. While the amplitude of corrugations is about 25% of the plate thickness, we hypothesize that it may play a role in increasing the plate toughness by adding geometric non-planarity in the crack path. This mechanism has been identified previously in several systems including graphene sheets[68] and rough faults[69]. We conjecture that this inclusion-patterned non-planarity may be playing a role in the toughness of biological composites such as mineralized collagen fibril. This is a topic of further investigation.

While the system investigated in this paper has several exciting features and potential applications, it does suffer from a number of limitations. For example, we have observed that the corrugation saturates beyond a certain value of stretch. Currently we are able to achieve maximum corrugation amplitude 25-30% of the fibril thickness. Moreover, due to the elasticity of the system the deformations are recovered upon removal of loads. While this may be a desirable property, it points to the fact that the loads have to be kept on the system during its operation in order to maintain the desired corrugation amplitude or channel geometry. While we do not see this as a problem in the envisioned applications, we acknowledge that this may be a limitation compared to other systems in which complex geometries are produced by plastic deformation or inelastic buckling. Finally, we have observed some stress concentration at the matrix-inclusion interfaces especially if the inclusion has sharp edges. We ran another simulation

in which we use inclusions with rounded corners. Our preliminary result suggests that, by rounding the inclusion corner the stress concentration is greatly reduced. This preliminary investigation suggests that the problem of stress concentration is controllable and will not have a detrimental impact on the performance of the system. We also note that the stretch magnitude considered here (<1.3) is relatively small and we do not expect cavitation phenomena to limit the response. Detailed investigation of the interfacial response as well as the potential for cavitation will be reported elsewhere.

We have numerically demonstrated the capability of modulating band gap structure in soft composites using sacrificial interfaces. While several approaches have been used previously to achieve this purpose, including designing of hierarchical composite structure[28], [42], triggered instabilities in monolithic periodic material[32], [70], and instability-induced interfacial wrinkling[33], [34], this is the first time, to the best of our knowledge, that sacrificial interfaces with controlled damage behavior is used to tune the band gap behavior.

The introduction of interfaces to a monolithic composite enriches the deformability of the system and provides a mean to alter the band gap structure. The interfacial deformation along composite fibrils is controlled by the inclusion pattern. Symmetrical aligned inclusion pattern results in the formation of parallel horizontal array of holes, while the staggered inclusion pattern leads to oblique orientation of holes. In both cases the composite microstructure is evolving gradually with the introduction of a new phase (i.e. voids). The softening introduced by interfacial damage

as well as the new diffraction patterns generated by the nucleation and growth of voids as a function of stretch, compete with the deformation induced stiffening of the hyperelastic composite and lead to the emergence of a complex pattern of multiple band gaps.

While we have not computed the transmission spectrum explicitly in this study, we hypothesize that the band gap evolution in our system is facilitated by both Bragg diffraction and local resonance. The interfacial channels represent a new periodic inclusion of degrading stiffness and irregular boundary geometry. The periodicity of the channels provides additional diffraction paths for wave propagations. Moreover, wave reflection and refraction at the channel/matrix interface is opposite in polarity to wave dynamics at the matrix/stiffer inclusion interface (Channel stiffness < matrix stiffness < inclusion stiffness) and this may contribute to local resonance.

In the current study, the composite is elastic throughout the deformation and damage is only localized to the interfaces between fibrils. With the use of self-healing interfaces[71], [72] , the phenomena we are describing here are completely reversible. Furthermore, even if the interface remains damaged, the channels nucleate and grow to complex irregular shapes that interfere with the wave propagation and cause more complex behavior and possibly more frequency band gaps than composites with regular holes[70], [73].

In general, band gaps of the composite fibril system tend to shift to higher frequency region as stretch level increases. Initial band gaps vanish after damage initialization and more and wider

band gaps appear as stretch level becomes higher and total separation within the channel regions occurs. No band gap shows up in the monolithic composite even with the same inclusion pattern as the layered composite. It is the interaction between the inclusion pattern and the sacrificial interfaces which manipulate wave diffraction and interference leading to the creation of multiple frequency band gaps. For the cases considered in this paper, we show that band gaps are generated in the low frequency range after total separation within the channel regions. More band gaps are observed in symmetrically aligned pattern than those in staggered pattern. Interfacial damage plays an essential role in the evolution of these band gaps. The more ductile interface delays the complete separation and prevents the appearance of band gap in lower frequencies.

A future extension of this study will involve investigation of different potential applications of controllable tension-induced corrugations. For example, the ability to control the void sizes and shapes may be very useful in fluid treatment applications and may be advantageous over filters with constant mesh size. The effect of tension-induced non-planarity in 3D plates on fracture toughness and surface roughness development warrants further investigation particularly in the context of biological composites. Further applications and optimization of the tunable band gap structure can be explored. For example, the emergence of multiple band gaps under large stretch may have applications in wave filtering, sound isolation, and vibration damping. Furthermore, the width of the band gaps may be maximized through topology optimization so that the tunable band gaps, observed in the current study, may extend over wider regions of frequencies. Finally,

the connection between band gap structure and the effective toughness of the composite material is a topic that requires further exploration. In particular, it may be possible, through careful designing of the inclusion pattern and sacrificial interfaces, to be able to control crack nucleation and propagation by varying the band gap structure in the composite as a function of deformation.

REFERENCES

[1] H. D. Espinosa, J. E. Rim, F. Barthelat, and M. J. Buehler, “Merger of structure and material in nacre and bone – Perspectives on de novo biomimetic materials,” *Prog. Mater. Sci.*, vol. 54, no. 8, pp. 1059–1100, Nov. 2009.

[2] G. M. Luz and J. F. Mano, “Mineralized structures in nature: Examples and inspirations for the design of new composite materials and biomaterials,” *Compos. Sci. Technol.*, vol. 70, no. 13, pp. 1777–1788, Nov. 2010.

[3] J. W. C. Dunlop and P. Fratzl, “Biological Composites,” *Annu. Rev. Mater. Res.*, vol. 40, no. 1, pp. 1–24, Jun. 2010.

[4] R. O. Ritchie, “The conflicts between strength and toughness.,” *Nat. Mater.*, vol. 10, no. 11, pp. 817–22, Nov. 2011.

[5] S. Weiner and H. D. Wagner, “THE MATERIAL BONE: Structure-Mechanical Function Relations,” *Annu. Rev. Mater. Sci.*, vol. 28, no. 1, pp. 271–298, Aug. 1998.

[6] I. Jäger and P. Fratzl, “Mineralized collagen fibrils: a mechanical model with a staggered arrangement of mineral particles.,” *Biophys. J.*, vol. 79, no. 4, pp. 1737–46, Oct. 2000.

[7] A. E. Elbanna and J. M. Carlson, “Dynamics of polymer molecules with sacrificial bond and hidden length systems: towards a physically-based mesoscopic constitutive law.,” *PLoS One*, vol. 8, no. 4, p. e56118, 2013.

[8] C. K. C. Lieou, A. E. Elbanna, and J. M. Carlson, “Sacrificial bonds and hidden length in biomaterials: A kinetic constitutive description of strength and toughness in bone,” *Phys. Rev. E - Stat. Nonlinear, Soft Matter Phys.*, vol. 88, no. 1, pp. 1–10, 2013.

[9] W. Wang and A. Elbanna, “Crack propagation in bone on the scale of mineralized collagen fibrils: Role of polymers with sacrificial bonds and hidden length,” *Bone*, vol. 68, no. 217, pp. 20–31, 2014.

[10] G. E. Fantner, T. Hassenkam, J. H. Kindt, J. C. Weaver, H. Birkedal, L. Pechenik, J. a Cutroni, G. a G. Cidade, G. D. Stucky, D. E. Morse, and P. K. Hansma, “Sacrificial bonds and hidden length dissipate energy as mineralized fibrils separate during bone fracture.,” *Nat. Mater.*, vol. 4, no. 8, pp. 612–616, 2005.

[11] N. Zhang, S. Yang, L. Xiong, Y. Hong, and Y. Chen, “Nanoscale toughening mechanism of nacre tablet,” *J. Mech. Behav. Biomed. Mater.*, vol. 53, pp. 200–209, 2016.

[12] B.-W. Li, H.-P. Zhao, Q.-H. Qin, X.-Q. Feng, and S.-W. Yu, “Numerical study on the effects of hierarchical wavy interface morphology on fracture toughness,” *Comput. Mater. Sci.*, vol. 57, pp. 14–22, May 2012.

[13] E. P. Chan, E. J. Smith, R. C. Hayward, and A. J. Crosby, “Surface Wrinkles for Smart Adhesion,” *Adv. Mater.*, vol. 20, no. 4, pp. 711–716, Feb. 2008.

[14] V. Janarthanan, P. D. Garrett, R. S. Stein, and M. Srinivasarao, “Adhesion enhancement in immiscible polymer bilayer using oriented macroscopic roughness,” *Polymer (Guildf).*, vol. 38, no. 1, pp. 105–111, 1997.

[15] B. Davies, A. King, P. Newman, A. Minett, C. R. Dunstan, and H. Zreiqat, “Hypothesis: bones toughness arises from the suppression of elastic waves.,” *Sci. Rep.*, vol. 4, p. 7538, Jan. 2014.

[16] V. B. Shenoy and D. H. Gracias, “Self-folding thin-film materials: From nanopolyhedra to graphene origami,”

MRS Bull., vol. 37, no. 9, pp. 847–854, 2012.

[17] A. R. Studart, "Biological and Bioinspired Composites with Spatially Tunable Heterogeneous Architectures," *Adv. Funct. Mater.*, vol. 23, no. 36, pp. 4423–4436, 2013.

[18] S. Xu, Z. Yan, K.-I. Jang, W. Huang, H. Fu, J. Kim, Z. Wei, M. Flavin, J. McCracken, R. Wang, A. Badea, Y. Liu, D. Xiao, G. Zhou, J. Lee, H. U. Chung, H. Cheng, W. Ren, A. Banks, X. Li, U. Paik, R. G. Nuzzo, Y. Huang, Y. Zhang, and J. A. Rogers, "Assembly of micro/nanomaterials into complex, three-dimensional architectures by compressive buckling," *Science (80-.).*, vol. 347, no. 6218, pp. 154–159, 2015.

[19] J.-H. Lee, C. Y. Koh, J. P. Singer, S.-J. Jeon, M. Maldovan, O. Stein, and E. L. Thomas, "25th Anniversary Article: Ordered Polymer Structures for the Engineering of Photons and Phonons," *Adv. Mater.*, vol. 26, no. 4, pp. 532–569, 2014.

[20] S. M. Peltola, F. P. W. Melchels, D. W. Grijpma, and M. Kellomäki, "A review of rapid prototyping techniques for tissue engineering purposes," *Ann. Med.*, vol. 40, no. 4, pp. 268–280, 2008.

[21] M. Maldovan and E. L. Thomas, *Periodic Materials and Interference Lithography*. Weinheim, Germany: Wiley-VCH Verlag GmbH & Co. KGaA, 2008.

[22] J.-H. Lee, J. P. Singer, and E. L. Thomas, "Micro-/nanostructured mechanical metamaterials.," *Adv. Mater.*, vol. 24, no. 36, pp. 4782–810, Sep. 2012.

[23] A. H. Aly and A. Mehaney, "Enhancement of phononic band gaps in ternary/binary structure," *Phys. B Condens. Matter*, vol. 407, no. 21, pp. 4262–4268, 2012.

[24] M. Maldovan, "Sound and heat revolutions in phononics.," *Nature*, vol. 503, no. 7475, pp. 209–17, 2013.

[25] M. M. Sigalas and E. N. Economou, "Comment on acoustic band structure of periodic elastic composites," *Phys. Rev. Lett.*, vol. 75, no. 19, p. 3580, 1995.

[26] C. Goffaux and J. Sánchez-Dehesa, "Two-dimensional phononic crystals studied using a variational method: Application to lattices of locally resonant materials," *Phys. Rev. B*, vol. 67, no. 14, p. 144301, 2003.

[27] Y. Achaoui, A. Khelif, S. Benchabane, L. Robert, and V. Laude, "Experimental observation of locally-resonant and Bragg band gaps for surface guided waves in a phononic crystal of pillars," *Phys. Rev. B*, vol. 83, no. 10, p. 104201, Mar. 2011.

[28] Y. Chen and L. Wang, "Tunable band gaps in bio-inspired periodic composites with nacre-like microstructure," *J. Appl. Phys.*, vol. 116, no. 6, p. 063506, 2014.

[29] C. Goffaux and J. P. Vigneron, "Theoretical study of a tunable phononic band gap system," *Phys. Rev. B*, vol. 64, no. 7, p. 075118, 2001.

[30] S. L. Vatanabe, G. H. Paulino, and E. C. N. Silva, "Maximizing phononic band gaps in piezocomposite materials by means of topology optimization.," *J. Acoust. Soc. Am.*, vol. 136, no. 2, pp. 494–501, 2014.

[31] O. Sigmund and J. S. Jensen, "Systematic design of phononic band-gap materials and structures by topology optimization.," *Philos. Trans. A. Math. Phys. Eng. Sci.*, vol. 361, no. 1806, pp. 1001–19, May 2003.

[32] K. Bertoldi and M. C. Boyce, "Wave propagation and instabilities in monolithic and periodically structured elastomeric materials undergoing large deformations," *Phys. Rev. B - Condens. Matter Mater. Phys.*, vol. 78, no. 18, 2008.

[33] S. Rudykh and M. C. Boyce, "Transforming wave propagation in layered media via instability-induced interfacial wrinkling," *Phys. Rev. Lett.*, vol. 112, no. 3, pp. 1–5, 2014.

[34] A. Bayat and F. Gordaninejad, "Switching band-gaps of a phononic crystal slab by surface instability," *Smart*

Mater. Struct., vol. 24, no. 7, p. 075009, 2015.

[35] Z. Liu, "Locally Resonant Sonic Materials," *Science (80-.).*, vol. 289, no. 5485, pp. 1734–1736, Sep. 2000.

[36] G. Wang, X. Wen, J. Wen, L. Shao, and Y. Liu, "Two-Dimensional Locally Resonant Phononic Crystals with Binary Structures," *Phys. Rev. Lett.*, vol. 93, no. 15, p. 154302, 2004.

[37] X.-P. Wang, P. Jiang, T.-N. Chen, and J. Zhu, "Tuning characteristic of band gap and waveguide in a multi-stub locally resonant phononic crystal plate," *AIP Adv.*, vol. 5, no. 10, p. 107141, Oct. 2015.

[38] M. S. Kushwaha, "Stop-bands for periodic metallic rods: Sculptures that can filter the noise," *Appl. Phys. Lett.*, vol. 70, no. 24, pp. 3218–3220, 1997.

[39] A. Khelif, P. A. Deymier, B. Djafari-Rouhani, J. O. Vasseur, and L. Dobrzynski, "Two-dimensional phononic crystal with tunable narrow pass band: Application to a waveguide with selective frequency," *J. Appl. Phys.*, vol. 94, no. 3, p. 1308, Jul. 2003.

[40] J. O. Vasseur, P. A. Deymier, A. Khelif, P. Lambin, B. Djafari-Rouhani, A. Akjouj, L. Dobrzynski, N. Fettouhi, and J. Zemmouri, "Phononic crystal with low filling fraction and absolute acoustic band gap in the audible frequency range: a theoretical and experimental study.," *Phys. Rev. E. Stat. Nonlin. Soft Matter Phys.*, vol. 65, no. 5 Pt 2, p. 056608, May 2002.

[41] M. S. Kushwaha, P. Halevi, L. Dobrzynski, and B. Djafari-Rouhani, "Acoustic band structure of periodic elastic composites," *Phys. Rev. Lett.*, vol. 71, no. 13, pp. 2022–2025, Sep. 1993.

[42] Y. Chen and L. Wang, "Multiband wave filtering and waveguiding in bio-inspired hierarchical composites," *Extrem. Mech. Lett.*, vol. 5, pp. 18–24, Dec. 2015.

[43] A. Khelif, A. Choujaa, S. Benchabane, B. Djafari-Rouhani, and V. Laude, "Guiding and bending of acoustic waves in highly confined phononic crystal waveguides," *Appl. Phys. Lett.*, vol. 84, no. 22, p. 4400, 2004.

[44] Q. Chen and A. Elbanna, "Tension-induced tunable corrugation in two-phase soft composites: Mechanisms and implications," *Extrem. Mech. Lett.*, vol. 4, pp. 26–37, 2015.

[45] L. R. G. Treloar, "Stresses and Birefringence in Rubber subjected to General Homogeneous Strain," *Proc. Phys. Soc.*, vol. 60, no. 2, pp. 135–144, Feb. 1948.

[46] "Applied Mechanics of Solids (A.F. Bower) Chapter 3: Constitutive laws - 3.5 Hyperelasticity." [Online]. Available: http://solidmechanics.org/Text/Chapter3_5/Chapter3_5.php. [Accessed: 16-Nov-2015].

[47] S. Swaminathan, N. J. Pagano, and S. Ghosh, "Analysis of Interfacial Debonding in Three-Dimensional Composite Microstructures," *J. Eng. Mater. Technol.*, vol. 128, no. 1, p. 96, 2006.

[48] S. C. Lee and K. T. Kim, "A densification model for powder materials under cold isostatic pressing—Effect of adhesion and friction of rubber molds," *Mater. Sci. Eng. A*, vol. 498, no. 1–2, pp. 359–368, Dec. 2008.

[49] R. N. Palchesko, L. Zhang, Y. Sun, and A. W. Feinberg, "Development of polydimethylsiloxane substrates with tunable elastic modulus to study cell mechanobiology in muscle and nerve.," *PLoS One*, vol. 7, no. 12, p. e51499, Jan. 2012.

[50] L. Brillouin, *Wave propagation in periodic structures; electric filters and crystal lattices.* [New York]: Dover Publications, 1953.

[51] M. Aberg, "The usage of standard finite element codes for computation of dispersion relations in materials with periodic microstructure," *J. Acoust. Soc. Am.*, vol. 102, no. 4, p. 2007, 1997.

[52] M. I. Hussein, "Reduced Bloch Mode Expansion for Periodic Media Band Structure Calculations," *Proc. Math. Phys. Eng. Sci.*, vol. 465, no. 2109, pp. 2825–2848, 2009.

[53] M. Guttag and M. C. Boyce, “Locally and Dynamically Controllable Surface Topography Through the Use of Particle-Enhanced Soft Composites,” *Adv. Funct. Mater.*, vol. 25, no. 24, pp. 3641–3647, 2015.

[54] S. Weiner and H. D. Wagner, “The Material Bone: Strucutre-Mechanical Function Relations,” *Annu. Rev. Mater. Sci.*, vol. 28, pp. 271–298, 1998.

[55] J. W. C. Dunlop and P. Fratzl, “Biological Composites,” *Annu. Rev. Mater. Res.*, vol. 40, no. 1, pp. 1–24, 2010.

[56] U. G. K. Wegst, H. Bai, E. Saiz, A. P. Tomsia, and R. O. Ritchie, “Bioinspired structural materials,” *Nat. Mater.*, vol. 14, no. 1, pp. 23–36, 2015.

[57] J. Aizenberg, V. C. Sundar, A. D. Yablon, J. C. Weaver, and G. Chen, “Biological glass fibers: Correlation between optical and structural properties,” *Proc. Natl. Acad. Sci. U. S. A.*, vol. 101, no. 10, pp. 3358–3363, 2004.

[58] R. F. Zollo, “Fiber-reinforced concrete: An overview after 30 years of development,” *Cem. Concr. Compos.*, vol. 19, no. 2, pp. 107–122, 1997.

[59] S. M. Abtahi, M. Sheikhzadeh, and S. M. Hejazi, “Fiber-reinforced asphalt-concrete - A review,” *Constr. Build. Mater.*, vol. 24, no. 6, pp. 871–877, 2010.

[60] S. Thomas and R. Stephen, “Rubber Nanocomposites: Preparation, Properties, and Applications,” *Rubber Nanocomposites: Preparation, Properties, and Applications*. 2010.

[61] M. Åberg and P. Gudmundson, “The usage of standard finite element codes for computation of dispersion relations in materials with periodic microstructure,” *J. Acoust. Soc. Am.*, vol. 102, no. 4, pp. 2007–2013, 1997.

[62] B. Hassani and E. Hinton, “A review of homogenization and topology optimization I - Homogenization theory for media with periodic structure,” *Comput. Struct.*, vol. 69, no. 6, pp. 707–717, 1998.

[63] H. Sun, S. Di, N. Zhang, and C. Wu, “Micromechanics of composite materials using multivariable finite element method and homogenization theory,” *Int. J. Solids Struct.*, vol. 38, no. 17, pp. 3007–3020, 2001.

[64] H. Ying, Y. Zhang, and J. Cheng, “Dynamic urea bond for the design of reversible and self-healing polymers,” *Nat. Commun.*, vol. 5, 2014.

[65] J. T. B. Overvelde and K. Bertoldi, “Relating pore shape to the non-linear response of periodic elastomeric structures,” *J. Mech. Phys. Solids*, vol. 64, no. 1, pp. 351–366, 2014.

[66] E. Hawkes, B. An, N. M. Benbernou, H. Tanaka, S. Kim, E. D. Demaine, D. Rus, and R. J. Wood, “Programmable matter by folding,” *Proc. Natl. Acad. Sci. U. S. A.*, vol. 107, no. 28, pp. 12441–12445, 2010.

[67] E. A. Peraza-Hernandez, D. J. Hartl, and R. J. Malak Jr., “Design and numerical analysis of an SMA mesh-based self-folding sheet,” *Smart Mater. Struct.*, vol. 22, no. 9, 2013.

[68] T. Zhang, X. Li, and H. Gao, “Designing graphene structures with controlled distributions of topological defects: A case study of toughness enhancement in graphene ruga,” *Extrem. Mech. Lett.*, vol. 1, pp. 3–8, Dec. 2014.

[69] E. M. Dunham, D. Belanger, L. Cong, and J. E. Kozdon, “Earthquake ruptures with strongly rate-weakening friction and off-fault plasticity, part 2: Nonplanar faults,” *Bull. Seismol. Soc. Am.*, vol. 101, no. 5, pp. 2308–2322, 2011.

[70] K. Bertoldi and M. C. Boyce, “Mechanically triggered transformations of phononic band gaps in periodic elastomeric structures,” *Phys. Rev. B*, vol. 77, no. 5, p. 052105, 2008.

[71] Z. L. Shen, M. R. Dodge, H. Kahn, R. Ballarini, and S. J. Eppell, “Stress-Strain Experiments on Individual

Collagen Fibrils," *Biophys. J.*, vol. 95, pp. 3956–3963, 2008.

[72] B. K. Ahn, D. W. Lee, J. N. Israelachvili, and J. H. Waite, "Surface-initiated self-healing of polymers in aqueous media.," *Nat. Mater.*, vol. 13, no. 9, pp. 867–72, Sep. 2014.

[73] J. O. Vasseur, P. A. Deymier, B. Djafari-Rouhani, Y. Pennec, and A.-C. Hladky-Hennion, "Absolute forbidden bands and waveguiding in two-dimensional phononic crystal plates," *Phys. Rev. B*, vol. 77, no. 8, p. 085415, 2008.